# Study of the breathing mode development in Hall thrusters using hybrid simulations

Federico Petronio, Alejandro Alvarez Laguna, Anne Bourdon, Pascal Chabert

# Study of the breathing mode development in Hall thrusters using hybrid simulations

Federico Petronio,[1,2] Alejandro Alvarez Laguna,[1] Anne Bourdon,[1] and Pascal Chabert[1]

[1)] *Laboratoire de Physique des Plasmas (LPP), CNRS, Sorbonne Université, École Polytechnique, Institut Polytechnique de Paris, 91120 Palaiseau, France.*

[2)] *Safran Spacecraft Propulsion, Electric Propulsion Unit, 27208 Vernon, France.*

(*Electronic mail: federico.petronio@lpp.polytechnique.fr)

(Dated: 26 January 2024)

We use a 2.5D hybrid simulation to study the breathing mode (BM) dynamics in Hall thrusters (HTs). This involves a 1D Euler fluid simulation for neutral dynamics in the axial direction, coupled with a 2D axial-azimuthal Particle-in-Cell (PIC) simulation for charged species. The simulation also includes an out-of-plane virtual dimension for wall losses. This setup allows us to replicate the BM's macroscopic features observed in experiments. A comprehensive analysis of plasma parameters in BM's phases divides it into two growth and two decay sub-phases. Examining 1D axial profiles of electron temperature, gas and plasma densities, and particle creation rate shows that an increase in electron temperature alone cannot sustain ionization. Ionization seems influenced by the spatial correlation between electron and gas densities and ionization rate coefficient. Investigating ion back-flow reveals its impact on modulating neutral flux entering the ionization region. The hybrid simulation's outcomes let us assess the usual 0D predator-prey model's validity and identify its limitations. The ionization and ion convection term approximations hold, but the gas convective term approximation does not. Introducing an alternative gas convective term approximation involving constant density ejection from the ionization region constructs an unstable BM model consistent with simulation results. In addition, this paper explores how varying the imposed voltage and mass flow rate impacts the BM. The BM frequency increases with imposed voltage, aligning with theoretical predictions. The mass flow rate variation has a limited effect on BM frequency, following the theoretical model's trend.

## I. INTRODUCTION

The development of Hall Thrusters (HTs) has undergone a great rise in recent years, following the renewed interest in space-based technologies[1]. The HTs use an $\mathbf{E} \times \mathbf{B}$ configuration to ionize a neutral gas and to accelerate outwards the created ions, so as to produce the thrust. These devices are formed by an annular channel, opened at one end. At the other end, which is closed by the high-voltage anode, the neutral gas is injected. The electrons that sustain the ionization are produced by a cathode which is usually at the channel exit. The $\mathbf{E} \times \mathbf{B}$ configuration makes the electrons drift azimuthally in the channel. The presence of this electron drift is at the origin of the growth of numerous instabilities[2,3]. In recent years, a large number of studies have dealt with the development and consequences of these instabilities[4–8]. However, the largest scale instability of HTs is not directly related to the $\mathbf{E} \times \mathbf{B}$ electron drift: it is a long-period (i. e., some tens of microseconds) ionization instability which is known as the breathing mode (BM)[9]. The BM leads to strong variations in the discharge current value and in all the plasma properties. Such variations clearly affect the overall performance of the thruster, by increasing the erosion at the walls and modulating the power absorption. In the first phase of the BM, the plasma density experiences a noticeable rise, to the detriment of the neutral gas density. This trend continues until the gas density reaches a sufficiently low level, at which point the plasma density growth reaches an unsustainable state. When this turning point is reached, the plasma density naturally subsides, allowing the neutral gas to repopulate. This cyclic process then sets the stage for a restart. Despite having a grasp of the fundamental BM concept, a precise and universally accepted explanation remains an open question.

One of the first models was proposed by Fife *et al.*[10], who considered a 0D predator-prey model for neutral gas and charged species (with several strong assumptions about the system length and boundary conditions). By linear perturbation analysis of the continuity equations of neutral gas and ions, one obtains a harmonic oscillator response of the system. However, this simple model does not predict the growth of the instability. Some other primary attempts to model the BM have been discussed by Morozov and Savelyev[11]. Hara *et al.*[12,13] have shown that, even if we consider a more complex system of 2 equations, the growth rate of the oscillation remains negative. Analyzing a system of 4 equations (the continuity for gas and ions, ions momentum conservation equation, and electron energy conservation equation), Hara *et al.*[12] found that if the electron energy is free to vary, the ionization oscillation might be unstable. However, numerical experiments[13] have shown

that in such a 0D system, the oscillations are always stable, i. e., the growth rate is negative. More recently, Lafleur and coworkers[14] have shown (using both theoretical arguments and numerical integration) that such 0D systems do not predict the growth of the BM, even when the temporal variation of the electron temperature is accounted for.

Using some 1D quasi-neutral hybrid simulations (i. e. kinetic ions, fluid electrons and neutrals), Boeuf and Garrigues[9] described the BM mechanism as a spatial fluctuation of the neutrals in the region next to the exhaust and showed that the BM frequency is related to the time needed from the neutrals to fill the ionization region. Chable *et al.*[15] found the origin of this mode in a Bunemans' type instability related to the coupling between electric field and ion current. Barral *et al.*[16,17] made several efforts to explain the origin of the BM, showing that this mode derives from the competition between the ionization and the neutral gas advection. In particular, in Ref.[16], Barral and Ahedo reported that the BM can be reproduced by a fully fluid 1D model and that the current and gas density define the plasma state. By some small perturbation analysis they also showed that the linear modes linearly growing in simulations could be explained theoretically. However, they highlighted the fact that non-linearities modify the frequency obtained with the perturbation approach. In more recent years, Lafleur *et al.*[14] proved with 1D fluid simulations that the primary cause of the BM is related to the electron temperature and electron power absorption, while the ion recombination at the anode has a negligible effect on the BM. Furthermore, Lafleur *et al.*[14] showed that anomalous mobility does not appear to be the primary trigger of the BM. Chapurin *et al.*[18,19] suggested that the characteristics of the BM depend on the thickness of the ion back-flow (towards the anode) region. Furthermore, they studied the sensibility of the BM on the chosen magnetic field and anomalous mobility profile. The results clarified that, for the neutral dynamics, the continuity and momentum equations (with constant temperature[20]) are sufficient to reproduce the BM mechanism. In a recent publication[21], the authors investigated the development of the BM utilizing a hybrid axial-radial code. They underscored the standing-wave nature of density oscillations and discussed the progressive wave structure concerning electron temperature. The BM was also studied in several experimental papers[22–25]. A review work on the BM was presented by Li-Qiu *et al.*[26].

Despite the great efforts and useful models that have been proposed throughout the years, a detailed analysis of the evolution of the parameters during a BM using a Particle-in-Cell (PIC) simulation is still missing. In particular, a PIC simulation allows us to capture detailed kinetic effects (i. e. that may not be as accurately represented in other simulation approaches) on the different quantities

having an impact on the BM. In this paper, we used a 2.5D hybrid code, LPPic, which uses a PIC description of the charged species, while solving the 1D Euler equations for the neutral gas[27]. The simulation of both the charged species dynamics and the gas dynamics allows us to reproduce the BM oscillations. In previous models of axial-azimuthal simulations, usually, the voltage is kept constant [28,29]. In this work, the PIC code is coupled to an RLC circuit that mimics the actual filter used by experimental devices[7]. This allows the anode voltage to vary and to reproduce the BM oscillation in a more realistic way.

The primary goal of this paper is to understand the relations between the varying parameters during a BM, taking advantage of the kinetic description of charged particles in our simulation. These observations will help discern which fluid approximations are valid, and which have to be improved. By rewriting the system of continuity equations for neutral gas and plasma under various assumptions, we demonstrate that it is feasible to replicate the BM oscillations using a 0D system that aligns with the findings of the hybrid simulation. The paper is organized as follows: Section II presents the code used for the simulations. Then, in Section III we analyze a given simulation in detail. First, we study the relations between the different parameters during a BM cycle, and later we discuss which BM models are consistent with our results. In particular, we challenge some of the models in the literature to determine to what extent their approximations are confirmed by the simulation discussed in the present work. Subsequently, in Section IV we analyze the limitations of the Fife's 0D system and we propose an alternative to it, which takes into account the results from the hybrid simulation. In Section V we present some results obtained by varying the input parameters in the simulations. In particular, we study the effect on the BM of variating the imposed voltage and neutral gas mass flow rate.

## II. DESCRIPTION OF THE PIC SIMULATION

### A. Simulation setup

The simulations are performed with a 2D-3V electrostatic, time-explicit hybrid code, LPPic, which has been extensively used to simulate HTs. Moreover, LPPic has notably taken part in two international benchmark studies involving radial-azimuthal[30] and axial-azimuthal[29] configurations. A detailed discussion of the code has been given in Refs.[7,27,31,32]. In the following, we sum up its main characteristics.

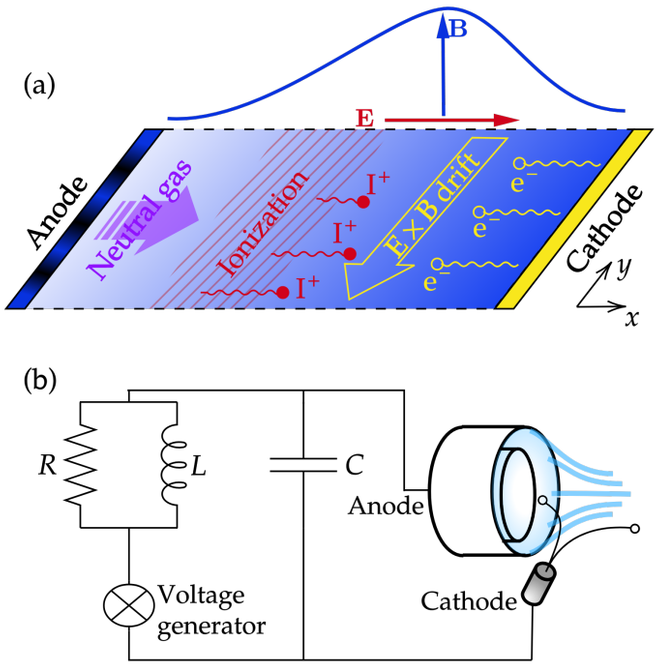


FIG. 1: (a) Axial-azimuthal simulation domain used in hybrid simulations. (b) Scheme of the electrical circuit modeled in the simulation.

In Figure 1 (a) we show a simplified scheme of the simulation domain. The spatial domain consists of a Cartesian mesh, with periodic boundary conditions along the azimuthal ($y$) direction. At the boundaries of the $x$ direction, we find the anode and the cathode. The cathode is grounded. At each time step, we inject a number of electrons to fulfill the quasi-neutrality conditions in the last cell[32]. The anode is at high voltage, and the imposed voltage is controlled by an external circuit, which is reported in Figure 1 (b). The circuit modeling is discussed in Ref.[7]. A magnetic field in the out-of-plane direction is imposed, constant in time, so as to recreate the $\mathbf{E} \times \mathbf{B}$ drift of electrons.

Collisions between charged species and neutrals are treated through a Monte Carlo collision (MCC) model employing the null-collision frequency method established by Vahedi and Surendra[33]. The MCC model self-consistently accounts for electron-impact ionization.

The neutral dynamics is solved with 1D Euler equations along the axial, or $x$, direction. The Euler equations are solved with an HLLC solver[34]. A fixed neutral flux rate is imposed at the anode, while open boundary conditions are imposed at the cathode boundary. The 1D Euler system

solved in LPPic is

$$\begin{cases} \partial_t \rho_g + \partial_x(\rho_g u_g) & = S_1, \\ \partial_t(\rho_g u_g) + \partial_x(\rho_g u_g^2) & = -\partial_x P_g + S_2. \end{cases}$$

In the previous expressions, $\rho_g$ is neutral density, $u_g$ is the neutral fluid velocity, $S_1$ and $S_2$ are the collisional source terms and $P_g$ is the neutral pressure. The neutral gas temperature is set to 640 K. More details about the solution of the neutral dynamics are given in Charoy *et al.*[27]. The terms $S_1$ and $S_2$ are calculated by counting the number of collisions between electrons and neutrals occurring in the MCC module.

A constant mass flow of neutral gas is injected at the anode. In addition to that, the anode boundary condition also accounts for neutrals produced from ion recombination at the anode. The set of equations described above deals with a flux $\Gamma_g = \rho_g u_g$, hence, to obtain the real mass flow rate in the device we need to define the device area.

In real HTs devices, the presence of the radial dimension plays an important role in determining the characteristics of the plasma. Inside the channel, a Bohm flux of particles leaves the simulation domain at the grounded thruster walls. Outside the channel, the dynamics in the plume is characterized by a high divergence angle[35]. However, since LPPic is a 2.5D code, the radial dynamics cannot be followed self-consistently and the model of the virtual-r direction will be detailed in the following section.

Finally, in order to relax the simulation numerical constraints[36] we used a permittivity scaling factor of 64, so that the time step and mesh size can be increased by a factor of 8. Even if the permittivity scaling may affect the plasma dynamics, it seems not to play a fundamental role in the BM development[27,37]. A comprehensive list of the simulation parameters, which draw inspiration from those of the PPS1350 by Safran, is provided in Table I. The azimuthal length $L_y$ is set to 4 cm to allow the full azimuthal development of the instabilities, as discussed in Ref.[7]. In the same reference one can find the representation of the magnetic field profile.

### B. The virtual-*r* model

To model the out-of-plane radial direction which is not self-consistently simulated, we rely on basic plasma physics concepts. In a bounded plasma, a charged sheath forms at the plasma-wall interface. The sheath is a spatially charged region, thus, an electric field directed towards the wall forms. This field accelerates the ions towards the wall and repels the electrons, reducing

the electron thermal flux that the walls absorb. In the case of dielectric walls, without secondary electron emission (SEE), the ion flux towards each wall can be obtained from Bohm theory[38] and reads

$$\Gamma_{\mathrm{i}} = hn\sqrt{\frac{k_B T_e}{m_i}}, \tag{1}$$

where $n$ is the plasma density in the center of the bulk and $h$ is the ratio between the plasma density at the sheath edge and the center[39]. The ion mass is denoted $m_i$ and the Boltzmann constant $k_B$. The electron flux is essentially a thermal flux, that can be expressed as

$$\Gamma_{\mathrm{e}} = \frac{n\bar{v}}{4}\exp\left(\frac{eV_f}{k_B T_e}\right),$$

with $\bar{v}$ the electron mean velocity of a Maxwellian distribution at the mean energy $3/2eT_e$ and $V_f$, that is negative, the potential difference between the wall and the bulk, named floating potential. The potential difference between the wall and the bulk is not calculated self-consistently in the simulations, thus, it is not possible to directly use this formula to extract the right number of electrons. Some previous works[40,41] proposed to set a constant value for $\Delta\Phi$ and absorb all the electrons with an energy larger than the given value. Nonetheless, this strategy has some drawbacks, as the potential difference between the wall and the bulk depends upon the plasma characteristics, which exhibit significant variation across the thruster channel. Moreover, suppose the absorption at the walls of electrons and ions follows two different mechanisms without any feedback between them. In that case, it is difficult to conserve the overall charge neutrality, which is mandatory in the case of dielectric walls. For this reason, we first calculate, and absorb radially, an ionic Bohm flux and then assume that the number of ions and electrons absorbed at the walls is the same. SEE can play a fundamental role in HT devices[11], however, as a first step, we decided to neglect the effect of SEE in our virtual radial direction. We leave the introduction of that effect to future work. In order to calculate the number of exiting particles from the flux[42], one needs to define the out-of-plane thickness of the simulation domain, $L_z$. In this first simulation, we considered a value of $L_z = 1.55\,\mathrm{cm}$, which corresponds to the real thickness of the thruster channel. The value of $h$ is set to $h = 0.5$, which is reasonable for this kind of plasmas[30]. All in all, since our model of the virtual radial direction accounts for the energy and particle losses to the walls, it truly improves the standard axial-azimuthal simulations in which the out-of-plane direction is not modeled.

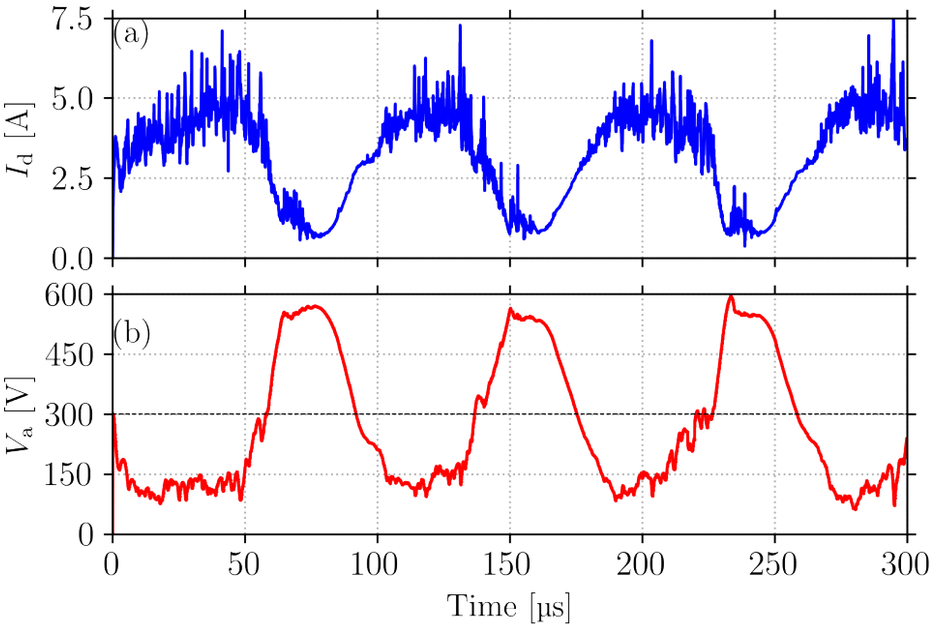


FIG. 2: (a) Current and (b) anode potential evolution.

## III. ANALYSIS OF THE BM DYNAMICS USING A PIC RUN

In this section, we analyze the BM dynamics using the axial-azimuthal PIC simulation with the virtual-$r$ described in Section II. The kinetic description of the charged species, coupled with the fluid description of neutral gas, allows us to reproduce the ionization process at the base of the breathing mode. In Figure 2 we report 300 µs of current evolution (a) and of the anode potential evolution (b) from the simulation. The addition of the virtual-$r$ decreases the average current value, but it does not notably affect the relative amplitude of the BM oscillations[37,42]. The dynamics in this figure show that the chosen time span allows the resolution of three full BM cycles. As one can see, both the current and the anode potential oscillate significantly. The oscillation frequency is around 12 kHz. In the following, we will study in detail the third current peak, between $\simeq$ 160 µs and $\simeq$ 250 µs. The good and regular shape of the BM peaks, also observed in Refs.[24,25], make this simulation particularly suitable for a detailed analysis of the mechanism driving the BM oscillation. The higher frequency oscillations visible in Figure 2 (a) are related to plasma resistive-like instabilities[43,44] in axial direction and are not the focus of this work. Some detailed discussion about these instabilities can be found in Ref.[8].

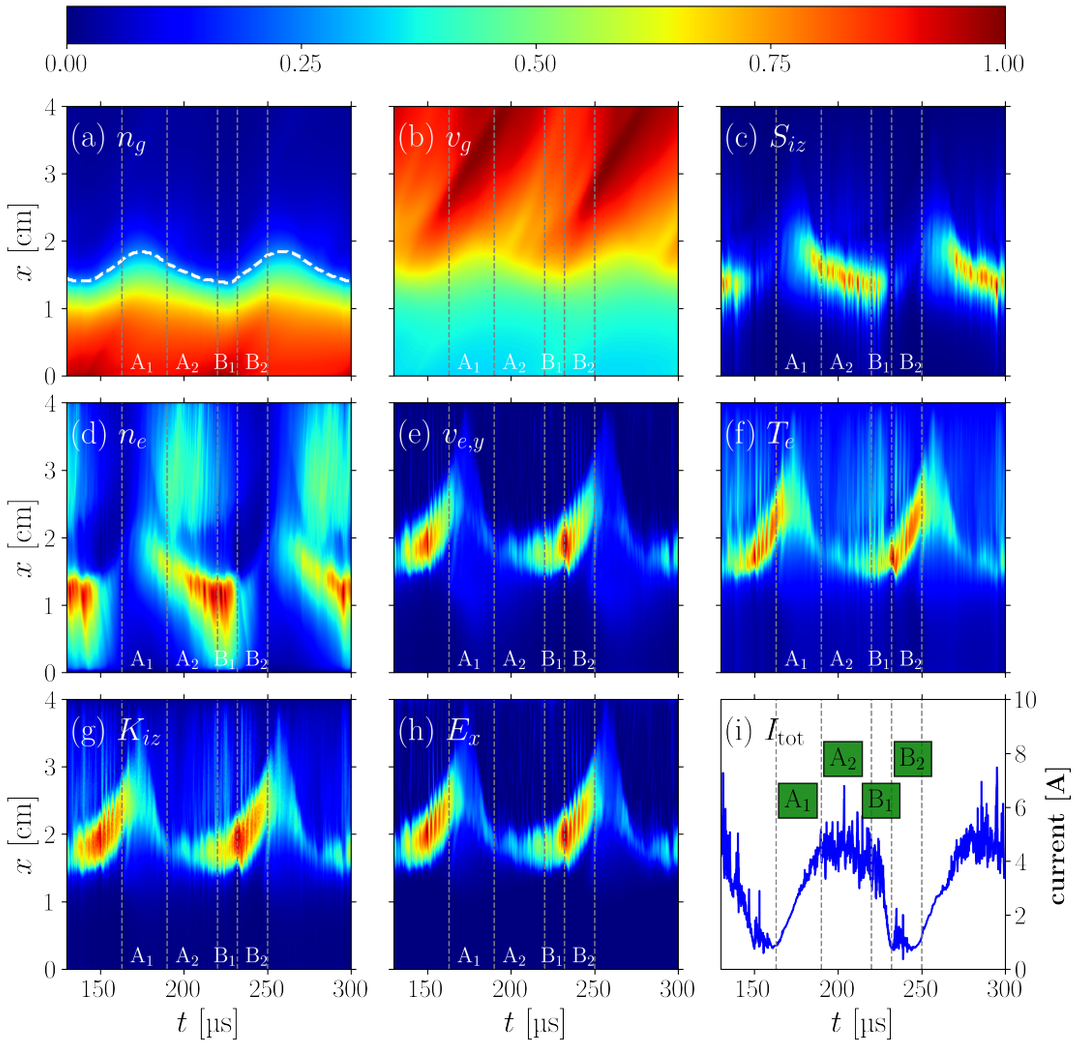


FIG. 3: Spatiotemporal evolution of (a) normalized gas density $n_g$, (b) gas speed $v_g$, (c) electron density production rate by ionization $S_{iz}$, (d) electron density $n_e$, (e) electron azimuthal speed $v_{e,y}$, (f) electron temperature $T_e$, (g) ionization rate coefficient $K_{iz} = S_{iz}/n_g n_e$, and (h) axial electric field $E_x$. The maps are obtained by averaging azimuthally at every time. The color scale is the same for all the plots. In (i) we show the total current evolution. The vertical dashed lines allow us to identify the four phases of the BM cycle.

### A. Analysis of breathing mode

In Figure 3, we show the temporal evolution of the axial profiles of some important plasma parameters averaged azimuthally: the normalized gas density $n_g$ (a), gas speed $v_g$ (b), electron density production rate by ionization $S_{iz}$ (c), electron density $n_e$ (d), electron azimuthal speed $v_{e,y}$

(e), electron temperature $T_e$ (f), ionization rate coefficient $K_{iz} = S_{iz}/n_g n_e$ and the axial electric field $E_x$ (g). The fluctuations of these quantities are crucial in the evolution of the BM, which is an ionization instability. Therefore, understanding their variations is essential for explaining the development of the BM. Each quantity is normalized by diving for its maximum in the simulation domain and in the considered time-span.

The ionization rate coefficient $K_{iz}(T_e)$ depends on the electron temperature $T_e$ as

$$K_{iz} = \frac{1}{n_e} \int_{\mathbb{R}^3} \sigma_{iz}(v) f_e(v) |\vec{v}| d\vec{v}, \tag{2}$$

with $v_{iz}$ the ionization threshold velocity (i. e., $v_{iz} = \sqrt{2e\mathscr{E}_{iz}/m_e}$, with $\mathscr{E}_{iz}$ the energy threshold for ionization in eV, $e$ the elementary charge and $m_e$ the electron mass), $\sigma_{iz}$ the ionization cross-section, and $f_e(v)$ the electron velocity distribution function, which is correlated to $T_e$. The ionization rate coefficient and the densities contribute to the ionization. The ionization $S_{iz}$, in the following named more precisely the electron density production rate by ionization, is given by

$$S_{iz} = n_g n K_{iz}(T_e). \tag{3}$$

The parameters, but $K_{iz}$, in Figure 3 are extracted directly from the code outputs. The values of $K_{iz}$ are calculated by reversing Eq. (3). We highlight that the parameters $S_1$ and $S_2$ of the neutral fluid equations are such that that $S_1 = -S_{iz}$ and $S_2 = -u_g S_{iz}$.

We propose to divide the BM cycle into four phases, as shown in Figure 3 (i). The vertical dashed lines separate the different phases. The first phase ($A_1$) corresponds to the first part of the growing BM phase, where the current grows significantly and has no high-frequency fluctuations. This phase is followed by $A_2$, which corresponds to the interval in which the current reaches a plateau and only high-frequency fluctuations are present. Then, the decreasing BM phase is divided into two parts: $B_1$ and $B_2$. In $B_1$ the current suddenly drops, while in $B_2$ the current is low, and high-frequency fluctuations are present. The cycle observed in this simulation has a rather slow dynamic: in several other cases the phases $A_2$ and $B_2$ are very short, or not even present. The characteristics of the BM change considerably when certain parameters, such as voltage, mass flow, etc., change.

In Figure 3 (a), we observe that the neutral density remains unperturbed during the BM cycle near the anode or in the plume, while it strongly varies in the mid-channel region. In $A_1$, where the current is increasing, we observe that the neutral density starts to decrease, while most of the neutral ionization occurs in $A_2$. This is the reason why we included $A_2$ in the BM growing phase:

it is a phase of high neutral gas ionization, where $S_{iz}$ is maximal. Then, when the BM decreasing phase starts in $B_1$, the phenomenon of neutral depletion is reversed: the neutral gas starts to repopulate. Most of the neutral repopulation occurs in $B_2$. The plasma density in Figure 3 (d) experiences a complementary behavior: the plasma starts from a low level at the beginning of $A_1$, then increases during $A_1$ and $A_2$, has a maximum in $B_1$, and drops in $B_2$.

A low number of electron-ion pairs are created during $A_1$, as one can notice by looking at $S_{iz}$ in Figure 3 (c). Most of the ionization events happen in $A_2$, when the neutral density is already decreasing. As a consequence, the plasma density peak is reached during $B_1$. In $B_2$ there is almost no ionization, and the plasma density remains low. The electron temperature decreases in $A_1$ and is low in the first part of $A_2$. Subsequently, in the second part of $A_2$ and in $B_1$, the electron temperature starts to increase. In $B_2$ the electron temperature is high, while the electron density is low. Before the ionization ignites again, the electron temperature has already dropped. So, the electron temperature corresponds to low ionization and vice versa (cf. Figure 3 (c) and (f)). However, $T_e$ is related to other plasma parameters: the axial electric field $E_x$ in Figure 3 (h) consequently and the electron azimuthal speed $v_{e,y}$ in Figure 3 (e). Indeed, when the electric field increases, the electron azimuthal drift (i. e., $v_{\mathrm{E}\times\mathrm{B}} = E/B$) does, and in turn, the averaged electron energy also increases. The ionization rate coefficient $K_{iz}$ in Figure 3 (g) is of course related to the electron temperature via Eq. (2).

As one can observe, the evolution of the electron density production rate is in phase with the evolution of the electron density amplitude. The electric field oscillation, in phase with the electron temperature, appears delayed with respect to the electron density oscillation. This is different from what was observed by Lafleur *et al.*[14] in a fluid simulation, in which the electric field increase was related to the electron density increase. During $A_1$, the increase in the electron density is sustained by the increase of the electron density production rate, and so on $n_e$ itself. The growth of $S_{iz}$ cannot be explained by the increase of $K_{iz}$, which diminishes, as $T_e$, in this phase. At the end of $A_2$, the neutral density is extremely low, which cancels out the electron density production rate $S_{iz}$. Nevertheless, for a short period, the charged species density growth is sustained by the increased temperature, which increases the ionization rate coefficient. However, this does not last long: even if $T_e$ remains high, in $B_2$ the electron density production rate and the density experience a sharp drop.

To better understand the ionization mechanism, we study the relationship between electron temperature, plasma, and gas densities, $K_{iz}$, and $S_{iz}$. We achieve this by examining how their ax-

ial profiles evolve. Figure 4 is divided into columns, each showcasing axial profiles of relevant plasma parameters during different times of the BM cycle. Each time instant, reported on top of each column, corresponds to the center of the four phases identified in Section III A. The primary objective of this figure is to elucidate the connections between densities, temperature, and ionization (including rate coefficient and density production).

Starting with the first row (Figure 4 (a-d)), we present axial profiles of electron temperature in the three simulation directions, along with the total temperature. Notably, the temperature profiles exhibit a consistent pattern across all three directions. They are relatively low near the anode and cathode, while reaching a peak at the channel exit (between 1.5 cm and 2.5 cm). Moving on to the second row (Figure 4 (e-h)), axial profiles of neutral gas density (depicted in brick color) and electron density (in green) are displayed. As anticipated, the electron density profile undergoes more pronounced changes over time compared to the neutral gas density. Continuing to the third (Figure 4 (i-l)) and fourth row (Figure 4 (m-p)), we provide profiles for $K_{iz}$ and $S_{iz}$, respectively.

As one can observe in the second row of Figure 4, the gas density profile varies slowly throughout a BM cycle. This behavior is better visualized in Figure 3 (a): the density remains high and nearly constant close to the anode, while it remains almost constant and close to zero within the plume. Meanwhile, in the ionization region located between these two extremes, the gas density demonstrates significant oscillations. To comprehend the underlying physical mechanism of these fluctuations, one should imagine the neutral gas mass oscillating back and forth around a fixed position, see for example the iso-density white dashed line in Figure 3 (a). During $A_1$ the neutral density first increases a little, then it starts to decline. The decline continues during $A_2$. During $B_1$ this mechanism reverses and we observe a partial increase of the neutral density in the channel. During $B_2$ we have a substantial neutral gas repopulating of the thruster channel.

In contrast, the electron density experiences more pronounced fluctuations. Notably, the density is low near the anode, progressively increases to reach its maximum within the thruster channel, undergoes a steep decline thereafter, and gradually rises within the plume. In the plume, the density exhibits minimal variation. In $A_1$ the plasma density is low and its axial gradient is minimal. During $A_2$ the plasma density increases and attains its plume maximal value. The density gradient at $x \simeq 1.5$ cm also increases. In $B_1$, corresponding to the BM decreasing phase, the density in the plume region drops, while it remains elevated in the internal part of the channel. In the last phase of the BM, $B_2$, the overall density is very low. However, we notice that it remains larger in the channel than in the plume.

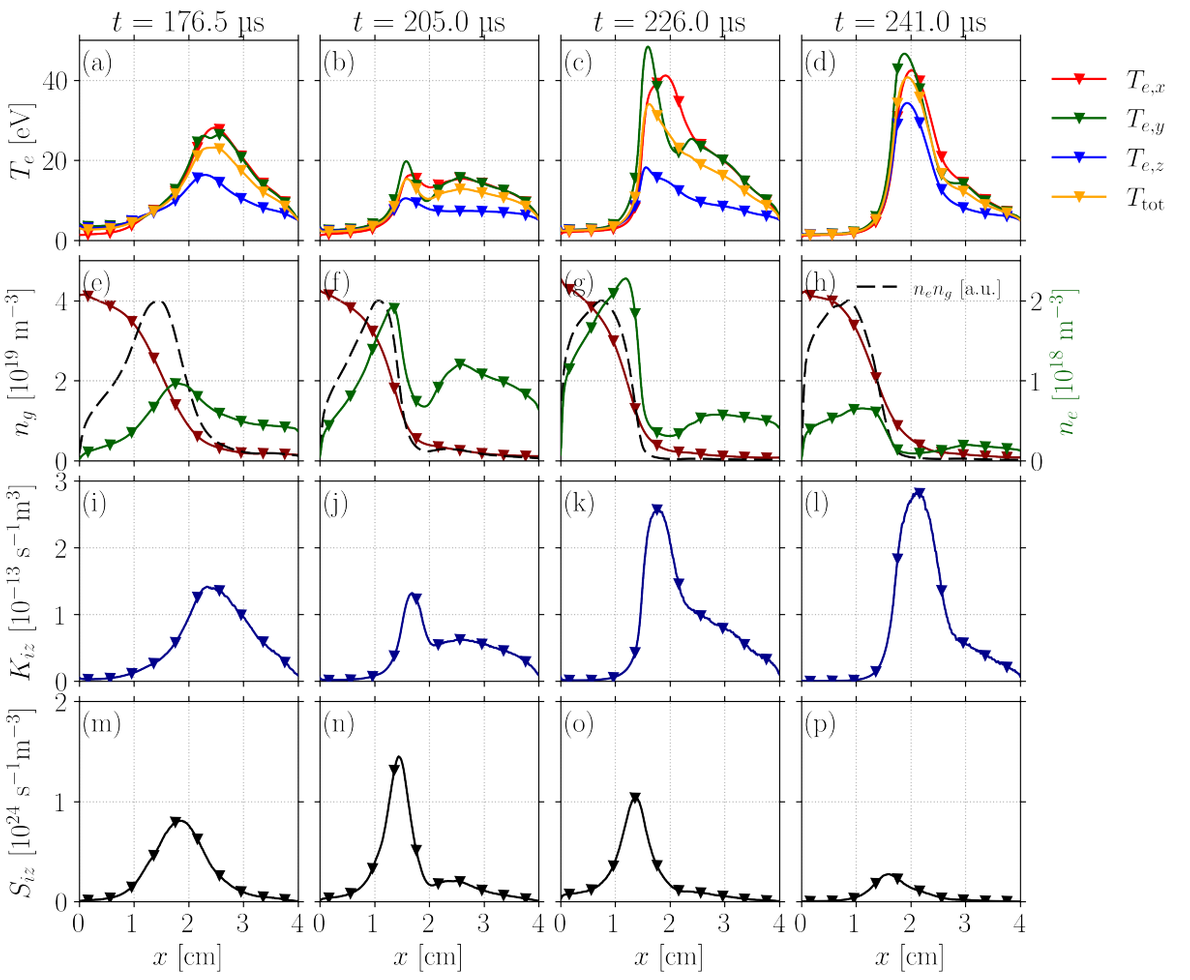


FIG. 4: Each column represents a time instant (indicated at the top of the first row). The first row (a-d) shows the electron temperature profiles along the three directions, as well as the total temperature. The second row (e-h) reports the gas density on the left axis, and electron density on the right one (the dashed line reports the product $n_e n_g$ in arbitrary units). The third row (i-l) shows the ionization rate coefficient $K_{iz}$, and the fourth (m-p) the electron density production rate $S_{iz}$. These data are extracted directly from PIC outputs.

In the third row of Figure 4, we show the ionization rate coefficient $K_{iz}$ profile evolution, which follows the temperature at all times. The profile of the ionization, alias $S_{iz}$, reported in the last row, results in differences from both the electron temperature and the density profiles. The amplitude of the ionization peak increases during the BM ascending phase, while diminishes greatly during the descending one. Nevertheless, the shape of the $S_{iz}$ peak remains very regular (i. e., with a bell form) during all phases of the BM.

It is therefore difficult to identify a positive feedback[14] between the electron density production rate and the electron temperature: when the temperature increases, the ionization rate coefficient $K_{iz}$ does, but the electron density production rate $S_{iz}$ does not. Moreover, in Figure 4 we observe that during $A_2$ the value of $S_{iz}$ increases significantly, although the temperature (and $K_{iz}$) does not rise. At the same time, the product $n_g n_e$ profiles in Figure 4 (e-h) are considerably different from the ones of $S_{iz}$. In the channel region at $x \simeq 1\,\text{cm}$, $n_g n_e$ is almost always maximal, but the density production rate is not very important at this axial position. A minor mechanism of positive feedback between the electron density production rate and the electron temperature could be present between $B_2$ and $A_1$, with the temperature decreasing slightly but shifting to the left so to increase the particle production. However, this mechanism is not sufficiently strong to be the BM driver. We also highlight that the electron population in the plume, which can be significant, does not contribute to the ionization. This is because the neutral gas is almost totally depleted in this region. All in all, particle production depends on the complex dynamics of both the gas and the plasma densities along with the ionization rate coefficient variations.

### B. Ion back-flow to the anode

Some recent work by Chapurin *et al.*[18] suggests that ion back-flow towards the anode is a fundamental mechanism contributing to the growth of the BM. In this section, we examine the evolution of the back-flow throughout the BM cycle in the previously presented simulation. Figure 5 (a) and (b) display the temporal changes in the ion velocity profile and selected profiles at specific times, respectively.

In Figure 5 (a) we observe that the ion back-flow region changes moderately its size during the different phases of a BM. The average dimension of this region is $\simeq 1.05\,\text{cm}$. During the BM growing phase $A_1$, this region reduces to $\simeq 0.78\,\text{cm}$, while it increases up to $\simeq 1.3\,\text{cm}$ during $A_2$. Despite the variation in the size of the back-flow region, Figure 5 (b) reveals that the velocity of the ions downstream seems to be significantly more influenced than the profile near the anode, which remains relatively stable. During the BM growing phase, the ion speed growth at the channel exit is relatively smooth. Subsequently, from $A_2$ at $x \simeq 2\,\text{cm}$ we observe a steep increase of the maximal ion speed.

To compare the number of ions flowing towards the anode and outside, we report in Figure 6 the evolution of the ion flux $\Gamma_{i,x}$ calculated at the anode $x = 0\,\text{cm}$ and the ion flux in the plume

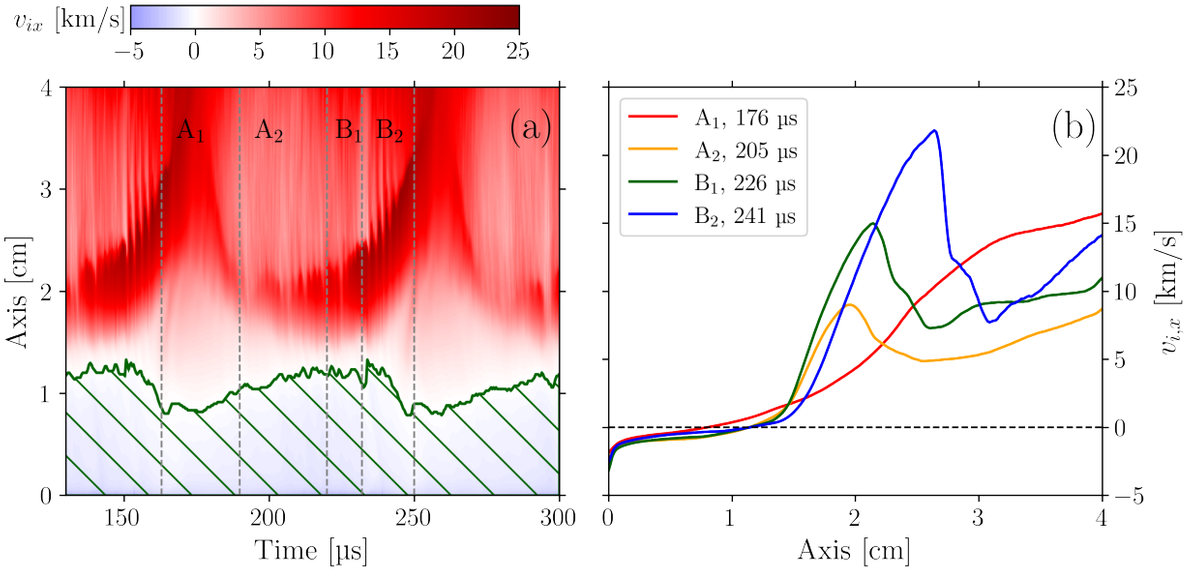


FIG. 5: (a) Spatio-temporal evolution of the ion axial velocity. The hatched area represents the part of the simulation in which the velocity is negative. (b) Four axial velocity profiles (calculated at selected times in the middle of each BM phase and shown in the legend).

(at $x = 3.5\,\mathrm{cm}$). We observe, as expected, that the outgoing flux is dominant all along the BM cycle. During $A_1$ the outgoing flux increases significantly, while the ingoing one is almost zero. During $A_2$ the outgoing flux starts to decrease, while oppositely the ingoing one increases. In $B_1$ the ingoing flux is no longer negligible if compared to the outgoing one, however, the net flux remains directed outwards. In $B_2$, which corresponds to the time of lowest ionization, both fluxes reduce significantly.

All in all, our simulation suggests that the advection of ions toward the anode is relatively weak, consistently remaining significantly lower than the ion stream flowing out of the thruster. Nonetheless, the ion recombination at the anode may indeed have a substantial impact on modulating the neutral flux entering the ionization region. This modulation, as we will delve into in Section IV, could be one of the primary mechanisms driving the BM.

## IV. THEORETICAL MODEL: PREDATOR-PREY 0D SYSTEM

Using a simple Lotka-Volterra scheme, Fife[10] modeled the mechanism underlying the BM. This model effectively describes the evolution of the main parameters of the BM. We discuss the limit of validity of this approximation in the following.

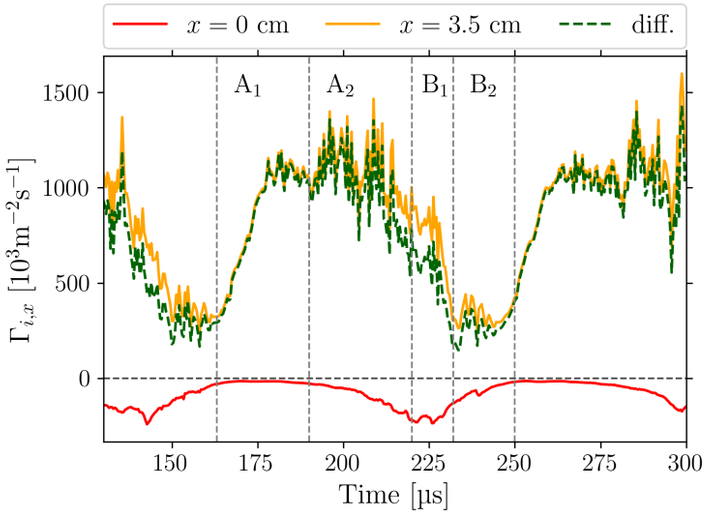


FIG. 6: Time evolution of the ion flux calculated at $x = 0\,\mathrm{cm}$ (red line) and at $x = 3.5\,\mathrm{cm}$ (yellow line). The green line represents the net flux.

The 1D continuity equations for the neutrals and the charged species are given by

$$\begin{cases} \dot{n}_g + \nabla \cdot (n_g v_g) &= -n n_g K_{iz}, \\ \dot{n} + \nabla \cdot (n v_i) &= +n n_g K_{iz}. \end{cases} \tag{4}$$

These expressions consider a quasi-neutral plasma evolving along the thruster axis. The ion velocity along $x$ is $v_i$, while the neutral velocity is $v_g$. The density variation due to ionization is expressed as a function of the ionization rate coefficient $K_{iz}(T_e)$, which varies along the thruster axis. The mass conservation equation is exact in standard PIC and fluid simulations. However, in the present case, it is interesting to study the effect of the azimuthal averaging and wall losses on the validity of these equations. Some comments about that are reported in Appendix A.

The 1D system (4) can be integrated on the ionization region, to obtain a 0D system. We assume that the neutral gas enters the ionization region, which has a thickness $L$, at a velocity $v_g^0$, which decreases to $v_g^L$ at the end of the region. The ions have low $v_i^0$ velocity at the beginning of the ionization region and are accelerated to $v_i^L$ at the end of it. The integrated continuity equations for neutrals and ions then read

$$\begin{cases} \dot{\bar{n}}_g + \dfrac{n_g^L v_g^L - n_g^0 v_g^0}{L} &= -\overline{n n_g K_{iz}}, \\ \dot{\bar{n}} + \dfrac{n^L v_i^L - n^0 v_i^0}{L} &= +\overline{n n_g K_{iz}}. \end{cases} \tag{5}$$

The averages over the ionization region of dimension $L = L_2 - L_1$ are expressed as

$$\bar{\alpha} = \int_{L_1}^{L_2} \alpha dx.$$

In the previous expressions, $n_g^0$, $n_g^L$, $n^0$, and $n^L$ are the neutral and plasma densities at the beginning and at the end of the ionization region, respectively. One should notice that in these expressions the superscript 0 corresponds to the position $x = L_1$, while the superscript $L$ corresponds to the position $x = L_2$. The ionization term is averaged over the ionization region and expressed as $\overline{nn_gK_{iz}}$. The quantities $\bar{n}$ and $\bar{n}_g$ represent the average plasma and neutral gas densities over the ionization region, respectively.

In this section, after having presented above the predator-prey 0D model, we compare the approximations of Fife's model with the results issued by the hybrid simulation. In particular, we discuss how the ionization length $L$ should be chosen. Subsequently, by analyzing the different possible approximations of the neutral gas equation convection term, we propose an alternative model that can better explain the dynamics of the BM.

### A. Choice of the ionization length

In the process of integrating the continuity equations, it is crucial to precisely define the boundaries of the ionization region. To achieve this, we have plotted the time-averaged axial profile of the ionization term, denoted as $S_{iz}$, in Figure 7 (a) (corresponding to the time-average of Figure 3 (c).). Notably, ionization levels are relatively low near the anode and cathode, while they peak in the middle of the channel. It is worth mentioning that fluctuations around the mean value are substantial when ionization levels are high, particularly near the peak of the bell curve. Conversely, these fluctuations are relatively small when ionization is low, such as near the anode and cathode.

An effective approach for delineating the ionization region is to create a plot that illustrates the integral of ionization from $x = 0$ to any given $x$. As illustrated in Figure 7 (b), a significant portion of the ionization primarily occurs in the central segment of the domain. By defining the boundaries of the ionization region at the 5% and 95% points of the total integrated ionization value, we establish a region with a length of 2.02 cm. From now on, we will model the evolution of the system within the region defined as $x \in [0.78, 2.80\,\text{cm}]$.

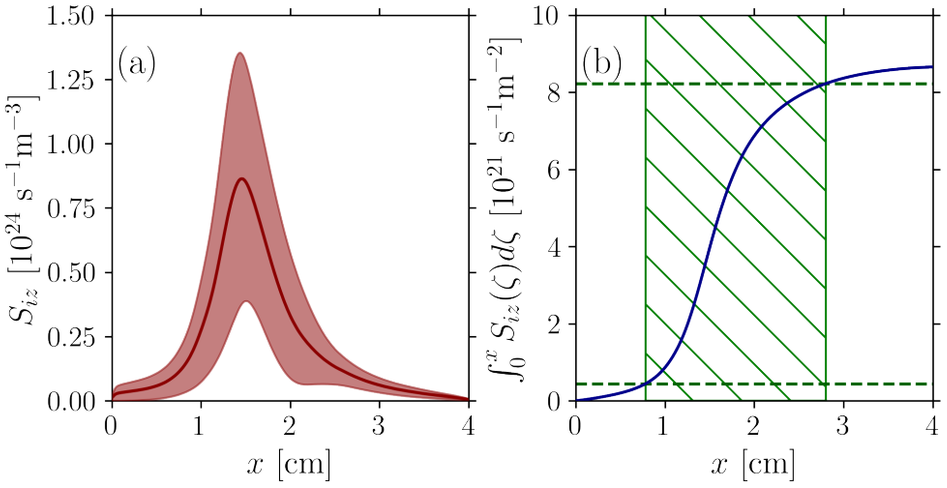


FIG. 7: In (a) we show the time-averaged axial profile on the ionization term $S_{iz}$. The shaded line represents the standard deviation from the mean value. In (b) we show the integral of the time-averaged axial profile of the ionization term $S_{iz}$. The horizontal dashed lines represent the 5% and the 95% of the integral ionization value.

### B. Discussion on the Fife model

The continuity equations system (5) cannot be solved analytically. Approximations are therefore necessary. As mentioned, the first attempt to simplify this model was made by Fife[10], who proposed an intuitive simplification of the ionization and convection terms. In both equations, the Fife approach reduces the ionization as

$$\overline{nn_gK_{iz}} = \bar{n}\bar{n}_g\tilde{K}_{iz}, \tag{6}$$

with $\tilde{K}_{iz}$ constant in time. To approximate the integral of the convective term, Fife considered that the neutral flux leaving the ionization region is negligible if compared to the entering flux. Similarly, he considered that the ion flux entering the ionization region is negligible if compared to the flux leaving the region. Moreover, he supposed that the neutral density at the entrance of the ionization region can be approximated by the average neutral density $\bar{n}_g$ and the ionic density leaving the ionization region can be approximated by the average ionic density $\bar{n}$. Thus, he wrote the convective terms as

$$\frac{n_g^L v_g^L - n_g^0 v_g^0}{L} \simeq -\frac{\bar{n}_g v_g^0}{L}, \tag{7}$$

for the neutrals, and

$$\frac{n^L v^L - n^0 v_i^0}{L} \simeq \frac{\bar{n} v_i^L}{L}, \tag{8}$$

for the ions. By substituting these approximations in Eq. (5), we obtain the system of equations

$$\begin{cases} \dot{\bar{n}}_g - \dfrac{\bar{n}_g v_g}{L} & = -\bar{n}\bar{n}_g \tilde{K}_{iz}, \\ \dot{\bar{n}} + \dfrac{\bar{n} v_i^L}{L} & = +\bar{n}\bar{n}_g \tilde{K}_{iz}. \end{cases} \tag{9}$$

If we consider small perturbations, the linearized system can be easily solved. We obtain the equation of a harmonic oscillator with frequency

$$\omega = \frac{\sqrt{v_g v_{i,x}}}{L}.$$

Even if the Fife model efficiently describes the evolution of the main BM parameters, the limits of validity of the approximations have not been fully discussed. Below, we challenge the approximations of the Fife model with some results issued from our simulation.

The approximation made to the ionization term can be studied by plotting the temporal evolution of the full term $\bar{S}_{iz} = \overline{n n_g K_{iz}}$ and of the approximated term $\bar{n}\bar{n}_g \tilde{K}_{iz}$. As before, terms $\bar{n}$ and $\bar{n}_g$ are the spatially averaged densities and we can easily calculate their temporal evolution from the hybrid simulation. The calculation of the constant ionization rate $\tilde{K}_{iz}$, on the contrary, requires further discussion. The first approach is to calculate it as the temporal average of the simulation parameter $K_{iz}(x,t)$ averaged over the ionization region, i. e., $\langle \bar{K}_{iz} \rangle_t$. An alternative approach would be to calculate it as the time average of the ratio of the spatially averaged ionization term and the product of the spatially averaged densities, i. e., $\tilde{K}_{iz} = \langle \overline{n n_g K_{iz}} / (\bar{n}\bar{n}_g) \rangle_t \doteq \hat{K}_{iz}$.

In Figure 8 we show the temporal evolution of the ionization term and of its two approximations. As can be observed, calculating the constant ionization term by taking the average of the simulation parameter $K_{iz}$ is not suitable; it leads to a significant overestimation of the value of $\bar{S}_{iz}$. Conversely, determining the constant ionization term as the ratio of the spatially averaged ionization term to the product of the spatially averaged densities is highly convenient. In this case, the value of $\overline{n n_g K_{iz}}$ closely aligns with the approximate term $\bar{n}\bar{n}_g \hat{K}_{iz}$. The reason behind this phenomenon can be understood by referring to the discussion in Section III A. It is evident that the ionization rate profile does not align with the density profiles; a high ionization rate does not necessarily correspond to a high particle production. It is interesting to note, however, that by reducing the constant ionization rate by a factor of $\langle \bar{K}_{iz} \rangle_t / \langle K_{iz} \rangle = 2.225$, we can obtain a good

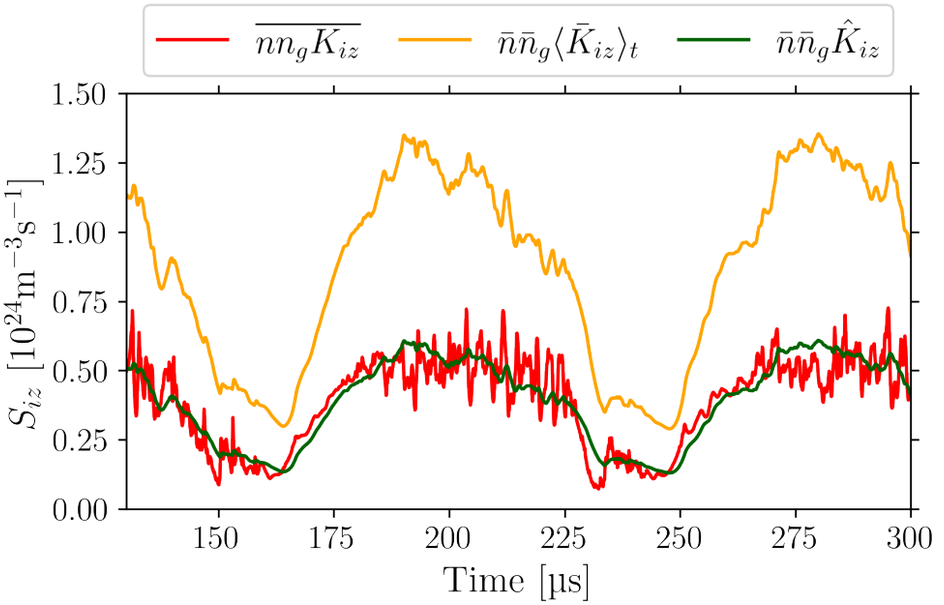


FIG. 8: Temporal evolution of the ionization term extracted by the PIC simulation and its approximation as in Eq. (6). The constant term $\langle\bar{K}_{iz}\rangle_t$ is calculated as the time average of the spatially averaged $K_{iz}$ in the ionization region. The term $\hat{K}_{iz}$ is calculated as the time average of the ratio of the spatially averaged ionization term and the product of the spatially averaged densities, e. g., $\langle\overline{nn_gK_{iz}}/(\bar{n}\bar{n}_g)\rangle_t$. Here we have: $\langle\bar{K}_{iz}\rangle_t/\hat{K}_{iz} = 2.225$.

approximation of the time evolution of the ionization term, as demonstrated by the green line in Figure 8.

Hence, we can deduce that Fife's proposed approximation of the ionization term is suitable for describing the ionization term across all time intervals. However, it is essential to note that the term $\tilde{K}_{iz}$ should not be regarded as the temporal and spatial average of the effective ionization rate derived from the simulation.

The approximation of the convective term can be examined by analyzing the temporal evolution of fluxes, densities, and velocities at various axial positions. Figure 9 illustrates how these parameters evolve at different axial positions for both the neutral gas (left column) and ions (right column). In Figure 9 (c), we can observe that the incoming neutral flux into the ionization region is significantly greater than the flux exiting it. However, it is worth noting that the incoming flux does not appear to be constant, while the flux leaving the ionization region exhibits a much smaller modulation. This behavior aligns with the modulation of neutral density at the entrance to the ionization region, as depicted in Figure 9 (a). The neutrals enter the ionization region with

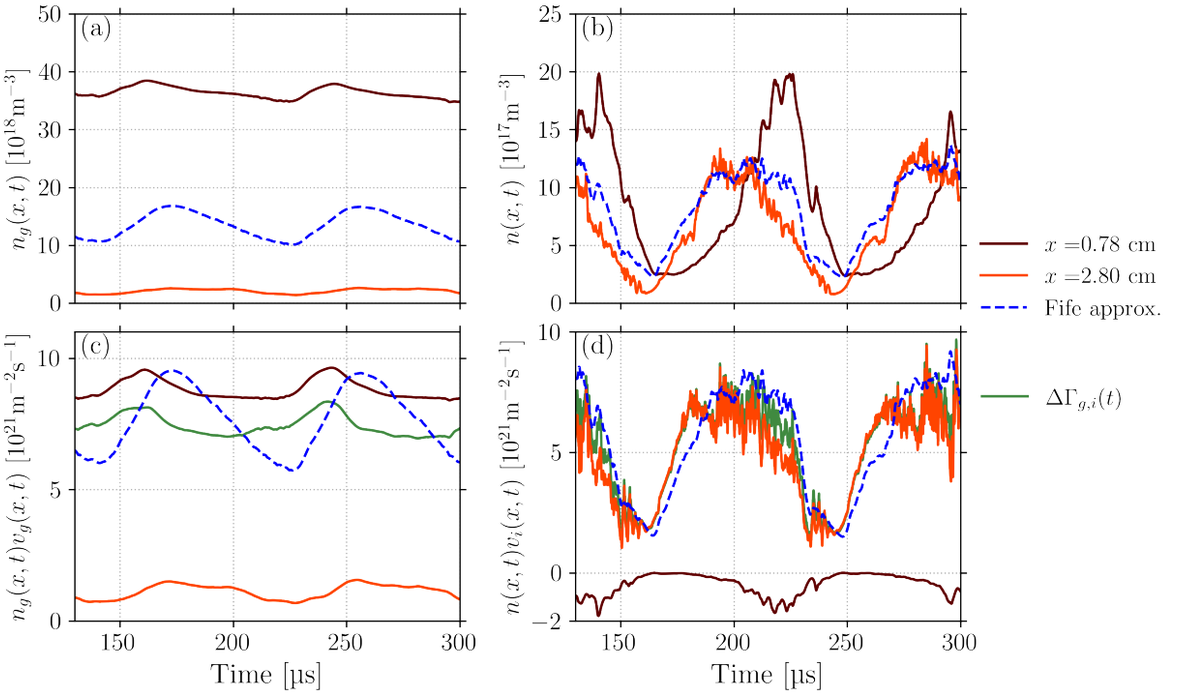


FIG. 9: For a fixed axial position (indicated in the legend on the right), we present the temporal evolution of various parameters as computed in the simulation. Specifically, we depict the temporal profiles of the (a) neutral density, (b) plasma density, (c) neutral flux, (d) and plasma flux. In these plots, the blue line represents the values calculated using the Fife approximation. The green lines, on the other hand, illustrate the actual integrated convective flux, denoted as $\Delta\Gamma_g(t) = \Gamma_g(x = 0.78, t) - \Gamma_g(x = 2.80, t)$ for the neutral gas in plot (c), and $\Delta\Gamma_i(t) = \Gamma_i(x = 2.80, t) - \Gamma_i(x = 0.78, t)$ for the ions in plot (d).

nearly constant velocity, undergo acceleration within the ionization region, and leave the region with a speed that varies with time.

Figure 9 (c) compares the Fife approximation of the neutral convective term detailed in Eq. (7) with the simulation integrated convective flux, denoted as $\Delta\Gamma_g(t) = \Gamma_g(x = 0.78, t) - \Gamma_g(x = 2.80, t)$. This figure demonstrates a notable disparity between the actual neutral convective term and its approximation. In this figure, the constant velocity utilized in the Fife approximation is determined as $v_g^0 = \langle \Delta\Gamma_g / n_g \rangle_t$. Similarly, in Figure 9 (a), one can observe that the average density significantly differs when compared to the density at the entrance of the ionization region. Consequently, these results suggest that the Fife approximation should be improved to better characterize the neutral convective term.

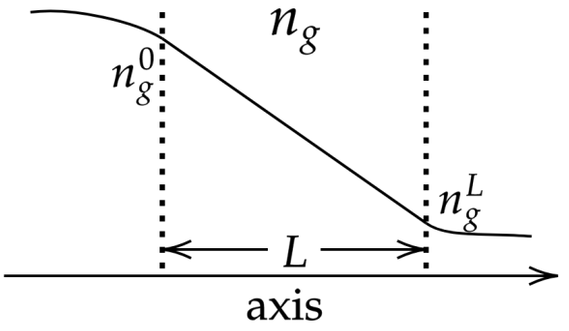


FIG. 10: The neutral gas density profile in the ionization region.

Conversely, in Figure 9 (d), it is visible that the Fife approximation, as described in Eq. (8), closely aligns with the actual ion convective term. Moreover, we observe a significant ion back-flow at the entrance of the ionization region, which could be responsible for the modulation of the ion flux and density at the anode. In this figure, the constant velocity used in the Fife approximation is determined as $v_i^L = \langle \Delta\Gamma_i / n \rangle_t$. In Figure 9 (b), we observe that the spatially-averaged density is close to the density at the exit of the ionization region. As a result, the Fife approximation proves to be appropriate for characterizing the ion convective term. In light of the discussion in Appendix A, it is important to consider the impact of the wall losses term in our analysis. Incorporating this term into the model is a relatively straightforward process. Given that both the convective term and the average losses are proportional to the average plasma density $\bar{n}$, integrating the wall losses term can be achieved by introducing an effective constant velocity $\tilde{v}_i^L = v_i^L + \alpha_w L$. Consequently, considering this term does not alter the structure of the ion continuity equation approximation.

### C. Alternative approximation of the predator-prey system

As demonstrated in the preceding section, the Fife approximation fails to accurately represent the evolution of neutral dynamics. In this section, we explore an alternative approximation that aligns with the simulation outcomes. We consider a neutral gas density profile, as depicted in Figure 10. At the entrance, the neutral density is denoted as $n_g^0$, while at the exit, it is designated as $n_g^L$. The average neutral density within the ionization region can be approximated as:

$$\bar{n}_g = \frac{n_g^0 + n_g^L}{2}. \tag{10}$$

We can assume the presence of a constant neutral injection velocity, denoted as $v_g^0$, and a constant ejection velocity, denoted as $v_g^L$, which are reasonable assumptions based on the findings presented in Figure 9.

To incorporate Eq. (10) into the predator-prey system, two assumptions can be made. Firstly, one can consider a constant injection density $n_g^0$, express the exiting density as

$$\frac{n_g^L v_g^L - n_g^0 v_g^0}{L} \simeq \frac{2\bar{n}_g v_g^L - n_g^0 (v_g^0 + v_g^L)}{L}, \tag{11}$$

and substitute this into Eq. (5).

In this scenario, the ion convective term and ionization term are approximated as in Fife's work. It is worth noting that this assumption aligns with the approach taken by Lafleur *et al.*[14] and Hara *et al.*[12,13], where the authors considered $v_g^0 = v_g^L = v_g$. However, in our case, we maintain the independence of $v_g^0$ and $v_g^L$. By applying a linear perturbation to this system, the resulting frequency is given by:

$$\omega_{1,2} = -\iota \frac{n_g^0 \tilde{K}_{iz}(v_g^L + v_g^0)}{2v_i^L} \pm \sqrt{\left(\frac{n_g^0 \tilde{K}_{iz}(v_g^L + v_g^0)}{2v_i^L}\right)^2 + \frac{n_g^0 \tilde{K}_{iz}(v_g^L + v_g^0)}{L} - \frac{2v_g^0 v_i^L}{L^2}}. \tag{12}$$

As one can see, this approximation produces a damped response of the system, consistent with observations made in previous references[13,14]. The symbol $\iota$ stands for the imaginary unit.

However, as we discussed in Section IV B, it was shown that the neutral density at the exit of the ionization region remains rather constant, whereas the density at the entrance does not. Hence, it is reasonable to set the density at the exit as $n_g^L$ and consider a variable density at the entrance, represented as $n_g^0 = 2\bar{n}_g - n_g^L$. Then, the convection term becomes

$$\frac{n_g^L v_g^L - n_g^0 v_g^0}{L} \simeq \frac{n_g^L (v_g^L + v_g^0) - 2\bar{n}_g v_g^0}{L}. \tag{13}$$

By applying this condition to the predator-prey system and utilizing the linear perturbation method, we derive the following frequency:

$$\omega_{1,2} = \iota \frac{n_g^L \tilde{K}_{iz}(v_g^L + v_g^0)}{2v_i^L} \pm \sqrt{\left(\frac{n_g^L \tilde{K}_{iz}(v_g^L + v_g^0)}{2v_i^L}\right)^2 - \frac{2v_g^0 n_g^L \tilde{K}_{iz}}{L} + \frac{(v_g^L + v_g^0)v_i^L}{L^2}}. \tag{14}$$

In this case, the steady-state values for the densities are

$$\begin{cases} \bar{n}_{g,\mathrm{ss}} = \dfrac{v_i}{L\tilde{K}_{iz}}, \\ \bar{n}_{\mathrm{ss}} = \dfrac{2v_g^0}{L\tilde{K}_{iz}} - \dfrac{(v_g^L + v_g^0)n_g^L}{v_i^L}. \end{cases} \tag{15}$$

From Eq. (14), it appears that the linear frequency response exhibits a positive growth rate. This implies that the modeled BM, when constructed in this manner, is unstable.

If we consider the approximation that $n_g^L \approx 0$, then the frequency response can be expressed as:

$$\omega_{1,2} = \imath 0 \pm \sqrt{\frac{(v_g^L + v_g^0) v_i^L}{L^2}}. \tag{16}$$

This result is similar to the solution previously found by Fife and discussed in Section IV B. However, the current derivation is more in line with the simulation results, as it incorporates the correct expression for the neutral density convection term.

If we assume that the velocity of the ions at the exit of the acceleration region is approximately $v_i^L \approx \sqrt{eV_\mathrm{a}/m_i}$, where $V_\mathrm{a}$ is the voltage applied at the anode and $m_i$ is the ion mass, we can derive the frequency of the BM as follows:

$$\omega_\mathrm{BM} \propto \sqrt{v_i^L} \propto \sqrt[4]{V_\mathrm{a}}. \tag{17}$$

Conversely, the frequency dependency on the mass flow rate reads

$$\omega_\mathrm{BM} \propto \sqrt{v_g^0} \approx \text{constant}. \tag{18}$$

It is important to note that when adjusting the neutral flux $Q$, the neutral density at the anode undergoes changes, whereas the expected impact on the neutral gas velocity is relatively minor.

It is interesting to compute the BM frequency and growth rate using the parameters from our simulation. In Figure 11, we present the results obtained by applying the simulation parameters to Eq. (14). The plasma properties were derived from the 2D simulation data and subsequently averaged azimuthally within the ionization region, as defined in Section IV A. Notably, the BM frequency observed in our simulation (e. g. $\approx 12\,\mathrm{kHz}$) closely aligns with the one predicted by the model and displayed in Figure 11 (a).

The growth rate of the BM in Figure 11 (b) appears to be lower than what is typically observed in the time spans covered by our simulations. However, it is not surprising that the BM is still observable in our simulation. Given that our simulations do not start from an equilibrium state, the BM is likely initiated by the initial perturbation, which could be relatively significant.

### D. Comparison of the different 0D models

In this section, we conduct a comparative analysis of the results obtained through the three 0D models discussed above. We consider the continuity equations for the neutral gas and the plasma,

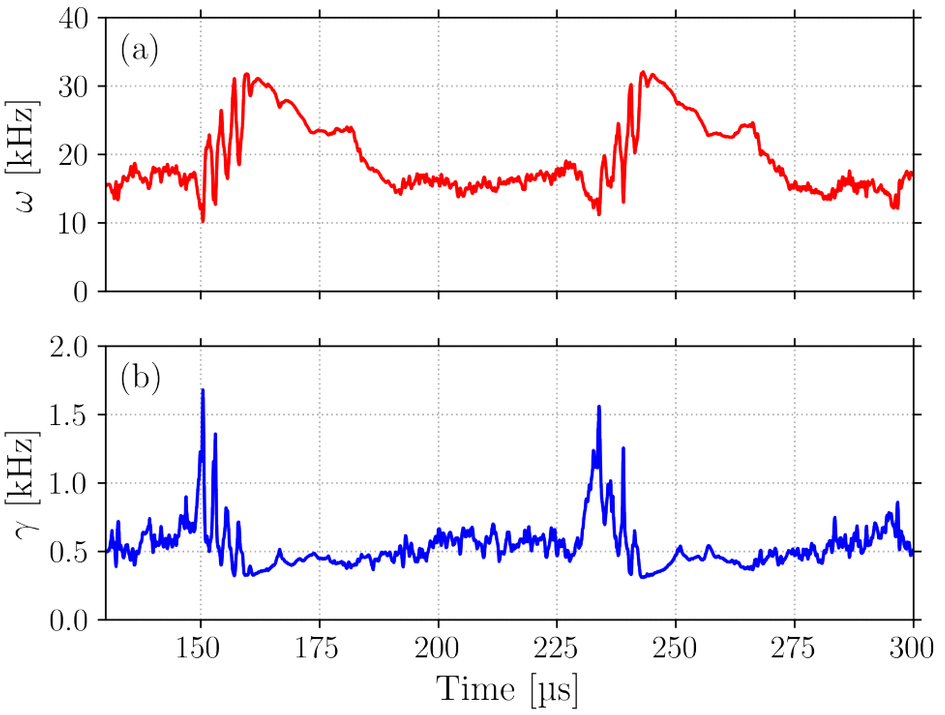


FIG. 11: Temporal evolution of (a) frequency and (b) growth rate, calculated injecting in Eq. (14) the plasma values extracted from the PIC simulation.

as outlined in Eq. (5), incorporating the convection terms as discussed earlier. By extracting the parameters from the simulation, we arrive at the numerical values provided in Table II.

Using the ordinary differential equations integrator provided by scipy.integrate, we solved the three systems discussed above. The results, obtained with the same initial conditions extracted from the hybrid simulation, are presented in Figure 12. As anticipated by the stability theory, the oscillations in the Fife model are neither damped nor growing. Since the initial condition does not correspond to the steady state, the oscillations persist. In the system with the second approximation (cf. Eq. (11)), the oscillations are damped, in accordance with stability theory. The third model, using the approximation in Eq. (13), exhibits instability, resulting in growing oscillations over time. The frequency of approximately 14 kHz of the BM in the first and third models closely matches that observed in the hybrid simulation (i. e., 12 kHz).

In summary, the modulation of the neutral density entering the ionization region appears to be linked to the growth of the BM. While the Fife model can replicate BM oscillations when the system does not start at equilibrium, it fails to reproduce the BM growth when it does. The presence of a modulated neutral density at the entrance of the ionization region is a necessary

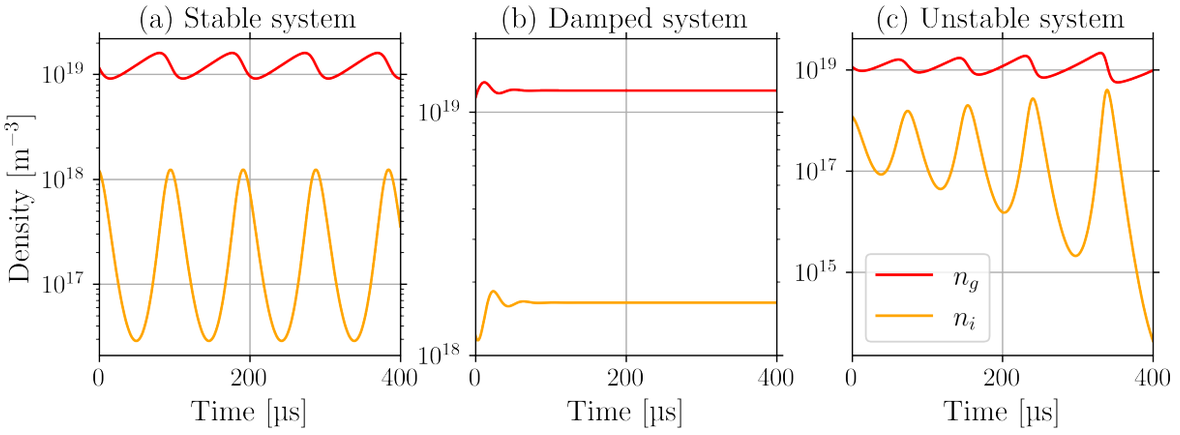


FIG. 12: Temporal evolution of neutral (red) and ion (orange) densities for the three 0D fluid models. (a) is obtained using the Fife approximation in Eq. (7), (b) is obtained using the approximation in Eq. (11), and (c) is obtained using the approximation in Eq. (13).

condition for BM growth. This condition corresponds to findings in a study by Chapurin *et al.*[18]: ion recombination at the anode and the resulting increase in neutral density at the entrance of the ionization region plays a crucial role in driving the BM growth.

## V. VARIATION OF THE INPUT PARAMETERS

In Section III we fully characterized the evolution of the plasma characteristics during a BM cycle. Here, we report the results of several simulations where we changed some input parameters. The simulation conditions are discussed in Section II and the input parameters are in Table I, when not otherwise mentioned. For each simulation, we kept constant the other parameters. The value of the virtual-$r$ thickness $L_z$ was set to 4 cm to decrease the wall losses in the cases with low voltage, or mass flow rate, so to ease simulation stability. We highlight that in the simulations presented in this section, the total power absorbed by the discharge is not kept constant: we are not controlling it. In our simulation, we fix the imposed generator voltage, then we let the simulated RLC circuit set the anode voltage (which then depends on the discharge current in the simulation).

### A. Effect of the voltage

The generator voltage is one of the parameters that can be more easily changed by a thruster user and it is known that the BM frequency generally increases with the increase of the voltage[23,45]. In the work by Gascon *et al.*[23], the authors observe experimentally that the frequency increases up to a given voltage value, and beyond that threshold, the BM frequency starts to decline. In this part, all the parameters are kept constant among the different cases, but the imposed DC supply voltage, i. e., $V_0$, which was varied from 200 V to 800 V.

In Figure 13 we show the evolution of the discharge current and the voltage at the anode for different values of the imposed DC supply voltage. These results clearly show that the plasma dynamics is strongly influenced by the imposed voltage. For example, the BM frequency increases with the voltage, as observed experimentally. Moreover, we observe that some high-frequency fluctuations in the current tend to disappear when we increase the imposed voltage. The amplitude of the current fluctuations varies significantly (i. e., in the range of $40\% - 80\%$ of the average current), but it is difficult to define a clear trend. Conversely, the fluctuations of the voltage have a more linear behavior: when we increase the voltage, the fluctuation amplitude drops.

Following the work of Fife[10], in Section IV we have written explicitly the dependency of the BM frequency on the voltage. The increase of the voltage causes an increase of the ion ejection velocity, e. g., $v_{i,x} \propto \sqrt{V_0}$, which in turn increases the BM frequency. By imposing a constant neutral flux, the neutral injection velocity is fixed and we should therefore observe the frequency scaling as

$$\omega_{\mathrm{BM}} \propto V_0^{1/4},$$

as mentioned in Eq. (17). By performing a Discrete Fourier Transform (DFT) of the discharge current, we obtain the spectra in Figure 14 (a). In this figure, we observe that in all the cases it is possible to identify a main BM frequency.

Figure 14 (b) shows the evolution of the BM frequency as a function of the imposed voltage. The results are subsequently fitted by a $\omega = aV_0^{1/4} + b$ law, with $a$ and $b$ two coefficients calculated with linear regression. The result shows that the trend follows the formula proposed in Section IV C. One should notice that when the voltage is low, the simulation experiences a strong transient, and the shape of the BM peaks changes significantly. So, in these conditions, several other mechanisms might influence the BM frequency.

The variation of the frequency for an increasing voltage is similar to the one measured by

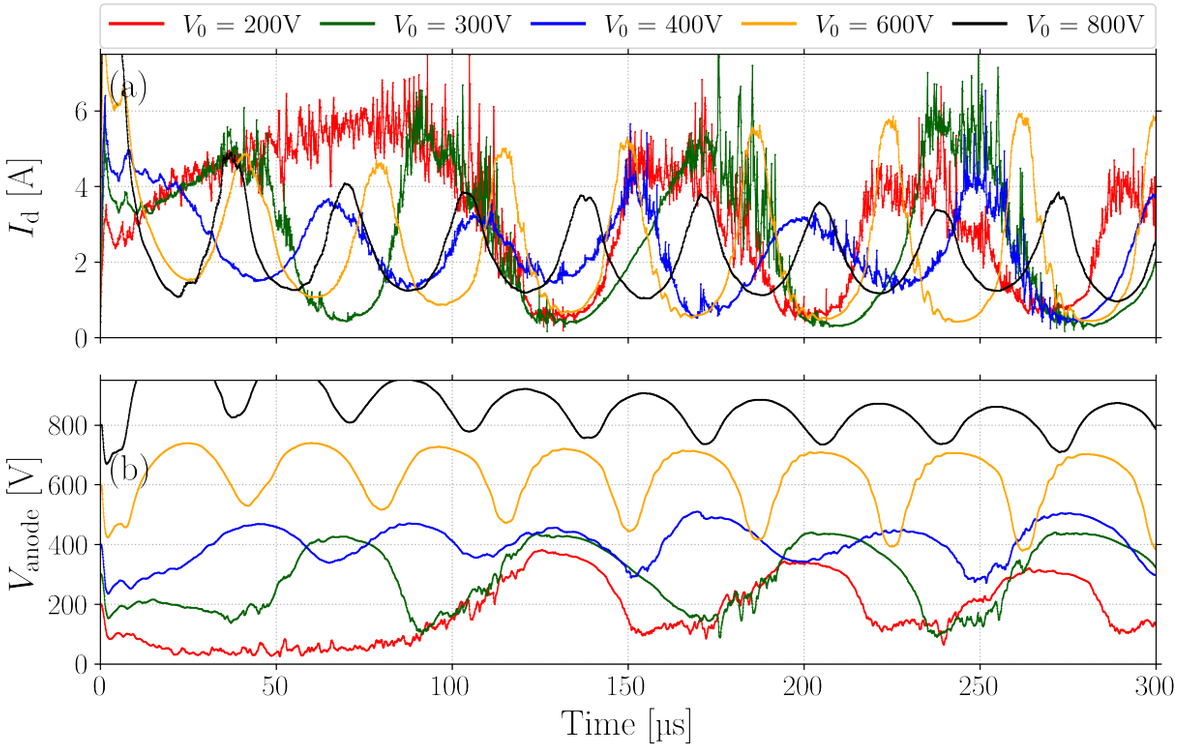


FIG. 13: (a) Discharge current and (b) anode potential as a function of time, for different voltages.

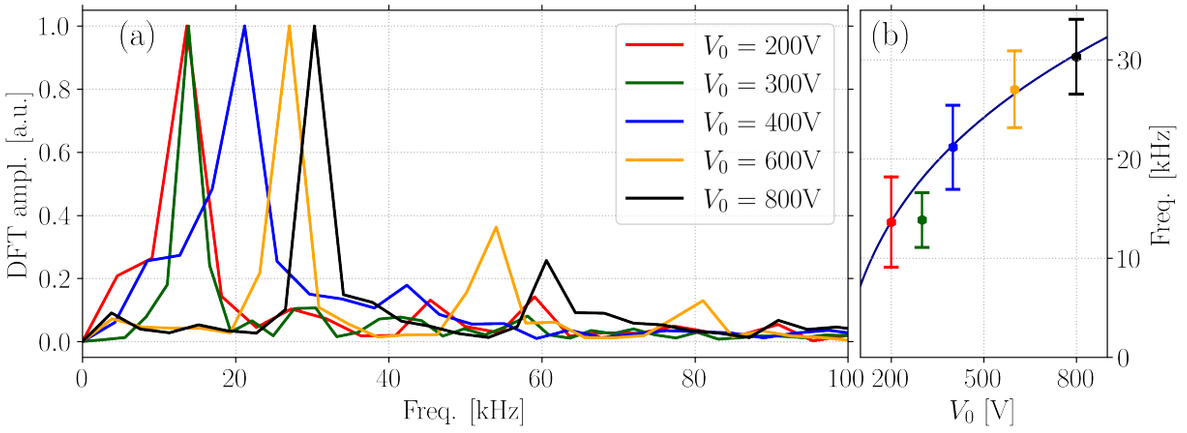


FIG. 14: (a) Normalized DFT of the current for different voltages. (b) Evolution of the BM frequency as a function of the voltage. The blue line shows a polynomial fit of type $\omega = aV_0^{1/4} + b$. The reported error bars cover $\pm\Delta f$ around the calculated value, with $\Delta f$ the frequency resolution of the DFT.

Gascon *et al.*[23]. However, they measured a frequency drop at high voltage, which is not happening in our simulations. The origin of this difference might be related to the modeling of the power supply or to the expansion of the plasma core and its interaction with walls, which are not modeled in our simulations. In the works of Ito *et al.*[45] and Lobbia and Gallimore[46], the authors find a rather steeper increase of the BM frequency with the voltage. Even if the cause of this phenomenon cannot be explained easily, it is plausible that the different discharge conditions (these results have been obtained in lower-power conditions) strongly affect the BM characteristics. However, there is a global agreement on the fact that the BM frequency increases with the voltage. The modeled circuit may have as well an effect on the BM, however, we believe that this affects more the amplitude of the BM than its frequency.

Figure 14 (a) shows that when we increase the voltage, we can detect higher order harmonics of the BM in the current, as it was observed by several experimental works[23,46,47]. The source of these harmonics remains unexplained.

### B. Effect of mass flow rate

One of the parameters that are usually modified to change the thruster working point is the neutral gas mass flow rate. In real devices, neutral gas is injected through some nozzles at the bottom of the thruster channel, in correspondence with the anode. The shape and distribution of these openings can have a non-negligible effect on discharge characteristics and thruster efficiency. However, in our bi-dimensional code, the nozzles are not modeled and the gas is uniformly injected into the system. The present analysis is performed by varying the neutral gas flow rate at the anode boundary in the 1D neutral fluid equations. As before, the simulation input parameters are the ones introduced in Section II. A virtual-$r$ of $L_z = 4\,\mathrm{cm}$ is used in these simulations in order to include some radial losses. The high cost of each simulation forced us to limit the physical time of each simulation: only a couple of BM periods are simulated for each test case.

In Figure 15 (a) we show the current evolution for five different values of the neutral gas mass flow rate, varied between $3\,\mathrm{mg/s}$ and $5\,\mathrm{mg/s}$. In Figure 15 (b) and (c) we show the BM frequency and amplitude for different values of the neutral gas mass flow rate, respectively. The BM frequency is calculated as the inverse of the time between consecutive peaks of the current since the DFT on such a limited amount of data was not satisfying. For $\dot{m} = 3\,\mathrm{mg/s}, 3.5\,\mathrm{mg/s}, 4\,\mathrm{mg/s}$ the frequency is calculated using two peaks, while for $\dot{m} = 5\,\mathrm{mg/s}$ the frequency is calculated using

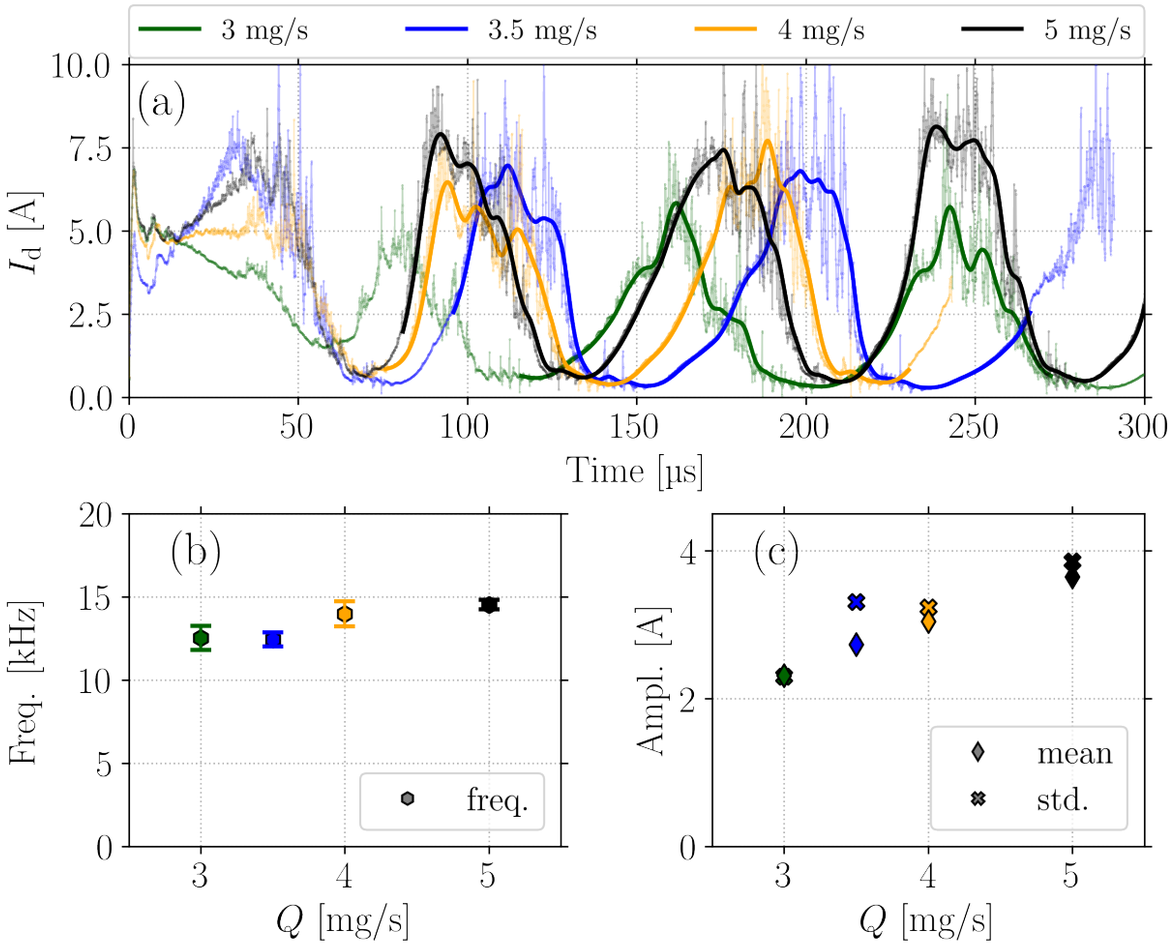


FIG. 15: From the current (a), we calculated the BM frequency (b), mean current, and the BM amplitude (c), for different values of the neutral gas flow rate. In (a) we show explicitly the filtered BM peaks. The error bars in (b) are computed as the standard variation of the frequencies calculated using different initial times for the start of the BM period.

several peaks. The error in the frequency measurement is therefore expected to be smaller for a higher mass flow rate. As an example, studying the blue line in (a), we observe that the current increase during the BM growing phase is much steeper at $t \simeq 100\,\mu s$ than at $t \simeq 250\,\mu s$. So, the choice of peaks might affect the frequency measurement, in a case like the present one, where a limited number of peaks can be used.

The results show that the BM frequency slightly increases with the mass flow rate, as observed experimentally[46]. In particular, in Eq. (18) we observe that the BM frequency is supposed to remain constant when the mass flow rate varies. The results in Figure 15 (b) report a behavior

compatible with the model prediction.

The BM amplitude is calculated as the current standard variation over a BM period and it is reported with the crosses in Figure 15 (c). The amplitude of the BM fluctuations appears to be strictly linked to the mean current: the amplitude of the fluctuations is as large as the current mean value.

## VI. CONCLUSIONS

The study involves examining how plasma parameters evolve during the BM using a 2D PIC simulation, which includes wall losses. The neutral gas dynamics is modeled with 1D fluid equations. Until now, there has been a lack of discussion about BM development in PIC simulations, due to the high cost of this type of simulation, which in our case was reduced by scaling the vacuum permittivity. However, the analysis of PIC results provides valuable insights into the development of the BM mode. Several important findings emerge from our study.

Firstly, the analysis of the plasma during a BM cycle showed that the BM can be divided into distinct phases: two during the current growth phase, denoted as $A_1$ and $A_2$, and two during the current decreasing phase, referred to as $B_1$ and $B_2$. The phases $A_2$ and $B_2$, which appear in the simulation studied here, in other simulations can be very shrunk or even might not be present. The division into phases allows us to better examine the temporal evolution of certain plasma parameters and to recognize the links between them.

By studying the ionization mechanism we noticed that particle creation is most prominent during phase $A_2$, while negligible production occurs during phases $B_1$ and $B_2$. The ionization rate coefficient, $K_{iz}$, is linked to the electron temperature, but its increment is not sufficient to sustain the charged particles density production rate, denoted here as $S_{iz}$. The evolution of $S_{iz}$ is influenced by the competition between neutral gas, plasma density, and the ionization rate coefficient. Notably, peaks in $S_{iz}$ and $K_{iz}$ are observed during different phases of the BM. For this reason, the temperature seems to have a less important impact on the BM dynamics, making the predator-prey model the fundamental mechanism driving the BM.

The enhancement of the electric field following the plasma density increase, present in fluid simulations, is not observed here. The increase of the electric field amplitude is delayed with respect to the increment of the density. Moreover, when the density is declining, the electric field still increases significantly.

The ion flow towards the anode, often referred to as back-flow, has small, but not negligible, temporal changes. The outward flow continues to dominate throughout the simulation. However, the advection of ions towards the back of the channel increases the ion recombination at the anode, with a consequent increase in the neutral density at the entrance of the ionization region, which appears to increase the growth rate of the BM.

Then, we analyzed the validity of the 0D approximation known as the Fife model. First, we defined using the hybrid simulation the spatial interval in which the ionization takes place. Then, we studied in detail the approximations made by Fife on the convective and ionization terms in the continuity equations. The approximation of the ionization term and the ion convective term appear to be successful. Conversely, the approximation of the neutral gas convection term does not appear to be valid. For this reason, we presented an alternative approximation of the neutral gas convection term, which is more consistent with the simulation results. In particular, we considered a variable neutral density entering in the ionization region. By using this approximation, the BM model is unstable and predicts a frequency close to the one observed in the simulation.

Subsequently, we used three different approximations of the convection term to solve the 0D system of equations. The results show that the Fife model can reproduce the BM oscillations when the system does not start at equilibrium. However, it fails to reproduce the BM growth. The presence of a modulated neutral density at the entrance of the ionization region is a necessary condition for BM growth. Nevertheless, when the system does not start in an equilibrium position, the BM oscillation also develops by simply considering the Fife model.

In the last part of the paper, we studied the BM evolution using several simulations in which we changed the input parameters. The trends we observed are similar to the ones that are found experimentally. Even if some differences persist (in particular at high voltage), we could identify the probable origin of the discrepancy. Furthermore, we have shown that the variation of the frequency with the voltage and of the mass flow rate is consistent at order zero with the predictions of the BM model proposed in the current work. This strengthens the idea that the simplified 0D model depicts the fundamental mechanism of the BM.

## ACKNOWLEDGMENTS

FP acknowledges financial support from a Safran Spacecraft Propulsion doctoral research award as well as from the Association Nationale de la Recherche et de la Technologie (ANRT) as

part of a CIFRE convention. This work has been partially funded by ANR (n$^o$ ANR-16-CHIN-003-01) and Safran Spacecraft Propulsion with the project POSEIDON. This work was granted access to the HPC resources of CINES under the allocations A0100510439 and A0120510439 made by GENCI.

## DATA AVAILABILITY

The data that support the findings of this study are available from the corresponding author upon reasonable request.

## Appendix A: Validity of the predator-prey system

The system of continuity equations written in Eq. (4) requires some further discussion. The simulation reproduces the neutral dynamics by solving the 1D axial Euler model for neutral, thus the 1D equation in Eq. (4) is automatically resolved. This is not the case for the 1D charged-species continuity equation, since plasma dynamics is reproduced by a 2D PIC simulation. It is therefore important to assess whether the averaging process to which kinetic dynamics of the plasma undergoes can be approximated by a 1D fluid model. In addition, it is interesting to study the effect of out-of-plane losses introduced in Section II B.

In Figure 16 (a) we show the spatiotemporal evolution of the ionization term $S_{iz} = nn_g K_{iz}$. The difference between the left-hand side (LHS) and right-hand side (RHS) of the ion continuity equation, as written in (4), is reported in (b). We observe that we can easily distinguish in the Figure 16 (b) the presence of the virtual walls absorbing some particles for $x < 2.5\,\mathrm{cm}$: in this region the error is much more significant.

In order to understand the origin of this error, we can introduce in the ion continuity equation a term that takes into account the losses at the walls (e. g., $L_w$). By counting in the simulation the number of ions effectively absorbed, we calculated $L_w$. We used this value in Figure 16 (c) to show that the error in the channel region ($x < 2.5\,\mathrm{cm}$) almost disappears when we include the wall losses. Thus, we can identify the lack of modeling of these losses as the main source of error in the ion continuity equation. Nevertheless, we note in Figure 16 (c) that there are time intervals in which the error is not completely negligible. In particular, the error is greatest in the channel during the BM $A_1$ phase, when azimuthal instabilities are strongest. It is therefore possible to

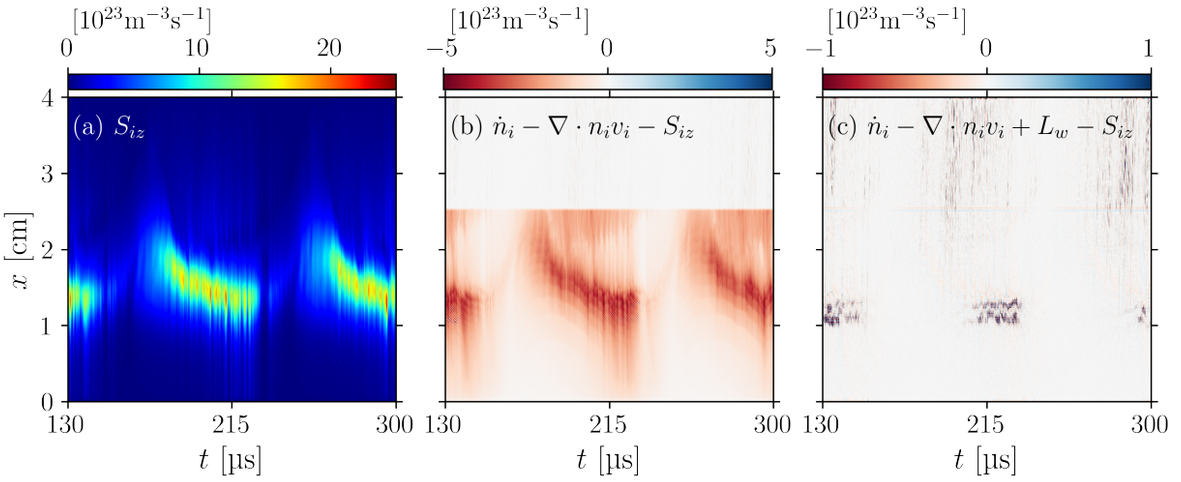


FIG. 16: (a) The particle creation term $S_{iz}$, (b) the error on the ion continuity equation, (c) the error in the ion continuity equation, including the wall losses term.

link the increase in error to the presence of kinetic instabilities, which cannot be modeled in the 1D fluid system. However, these kinetic effects seem to be of minor importance, since the error remains rather small.

We estimate the mean error related to the wall losses by averaging the difference among the LHS and RHS of the ion continuity equation (without the wall loss term) within the channel (i. e., $x \leq 2.5\,\mathrm{cm}$). In Figure 17 (a) we show the temporal evolution of mean error and the mean plasma density in the channel. The modeled radial losses are proportional to the density, thus it is not surprising to notice that there is a strict correlation between the mean error in the continuity equation and the mean plasma density. In Figure 17 (b), we report the ratio between the error in the continuity equation and the average density. As one can notice, this ratio does not vary significantly in time.

The quantity in Figure 17 (b) is homogeneous to a frequency, thus we can rewrite the wall losses term $L_w \approx \alpha_w n_i$, where $\alpha_w$ represents a loss frequency due to the presence of the walls. We can then rewrite the continuity equation as

$$\dot{n} + \nabla \cdot (n v_{i,x}) = n n_g K_{iz} - n \alpha_w. \tag{A1}$$

Now, we can calculate the evolution of the error in the case of the different expressions of the continuity equation. In Figure 17 (c) we show the relative error as the average of the difference of the LHS and RHS of the continuity equation when: no wall losses are considered in the equation (green), correct wall losses are considered in the equation (purple) and when the model in Eq. (A1)

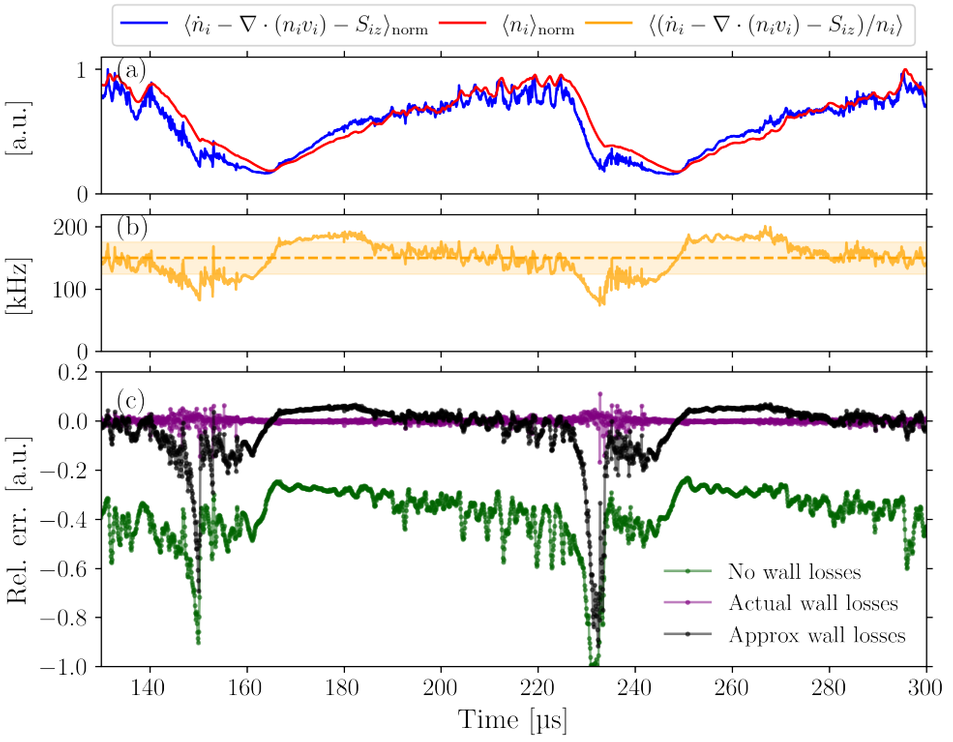


FIG. 17: (a) Error in the ion continuity equation (blue) and the mean ion density (red). Both these quantities are spatially averaged within the thruster channel and normalized. (b) Ratio between these quantities. The shaded area represents a standard deviation from the mean value. (c) Temporal evolution of the average relative error as the spatial (limited to the channel) average of the difference of the LHS and of the RHS of the plasma continuity equation. The relative error is obtained by dividing by the average value in the channel of $S_{iz} = nn_g K_{iz}$ at each time. The green line represents the standard continuity equation without wall losses, the purple includes the losses calculated from the simulation outputs and the black considers a loss term as in Eq. (A1), with $\alpha_w$ the time average of the value in (b).

is used (black). Consistently with Figure 17 (b), the value of $\alpha_w$ is chosen as the time average of $\langle (\dot{n}_i - \nabla \cdot (n_i v_i) - S_{iz})/n_i \rangle$, i. e., 150 kHz. Each error in Figure 17 (c) is divided by the average value of $S_{iz}$ in the channel.

The temporal fluctuations of the errors in Figure 17 (c) lead to some additional observations. Firstly, it is evident that the average error is significant when we do not account for wall losses. However, when we incorporate the simulation outputs that consider losses, the absolute error diminishes, resulting in a small null-average error. When we use the model described in Eq.(A1),

we observe a substantial reduction in the error, although some deviation from zero persists, particularly during the phases $B_1$ and $B_2$ introduced in Section III A. During these phases, the increase in the relative error is likely related to the drop in the absolute value of $S_{iz}$ as depicted in Figure 16 (a). In conclusion, we have shown that to model the results of the PIC simulations, the 1D ion continuity equation has to take into account a wall loss term proportional to the plasma density.

TABLE I: Operating and numerical parameters used in PIC simulations.

| Physical parameters | Symbol | Value | Unit |
|---|---|---|---|
| Gas | | Xenon | (-) |
| Radial magnetic field (max) | $B$ | 170 | G |
| Imposed voltage | $V_a$ | 300 | V |
| Cathode voltage | $V_c$ | 0 | V |
| Axial length | $L_x$ | 4 | cm |
| Azimuthal length | $L_y$ | 4.08 | cm |
| Radial length | $L_z$ | 1.55 | cm |
| Initial plasma density | $n_0$ | $5 \times 10^{18}$ | $m^{-3}$ |
| Initial electron temperature | $T_e$ | 1 | eV |
| Initial ion temperature | $T_i$ | 0.05 | eV |
| Neutral mass flow rate | $\dot{m}$ | 5 | $mg\,s^{-1}$ |
| Thruster section | $Area$ | $3.768 \times 10^{-3}$ | $m^2$ |
| Cathode injection temperature | $T_e^{cath}$ | 5 | eV |
| Resistance | $R$ | 60 | $\Omega$ |
| Inductance | $L$ | 4.4 | mH |
| Capacitance | $C$ | 15 | nF |
| Simulation parameters | | | |
| Time step | $\Delta t$ | $1.6 \times 10^{-11}$ | s |
| Cell size | $\Delta x = \Delta y$ | $1.6 \times 10^{-4}$ | m |
| Number of cells | $x_{\max} \times y_{\max}$ | $250 \times 255$ | (-) |
| Initial number of particles per cell | $N/NG$ | 400 | particles/cell |
| Macro-particles weight factor | $q_f$ | $64 \times 10^6$ | $m^{-1}$ |
| Number of iterations between outputs | $N_a$ | 5000 | (-) |
| Permittivity scaling | $\alpha^0$ | 64 | (-) |

| Parameter | Value |
|---|---|
| $n_g^0$ | $3.64 \times 10^{19}\,\mathrm{m}^{-3}$ |
| $n_g^L$ | $2.05 \times 10^{18}\,\mathrm{m}^{-3}$ |
| $n_i^0$ | $8.42 \times 10^{17}\,\mathrm{m}^{-3}$ |
| $n_i^L$ | $6.75 \times 10^{17}\,\mathrm{m}^{-3}$ |
| $v_g^0$ | $2.42 \times 10^{2}\,\mathrm{m/s}$ |
| $v_g^L$ | $5.38 \times 10^{2}\,\mathrm{m/s}$ |
| $v_i^L$ | $9.24 \times 10^{3}\,\mathrm{m/s}$ |
| $L$ | $2.03 \times 10^{-2}\,\mathrm{m}$ |
| $K_{iz}$ | $3.72 \times 10^{-14}\,\mathrm{m}^3/\mathrm{s}$ |

TABLE II: Parameters values used in the 0D models, obtained by averaging in the hybrid simulation over time and over the ionization region.

## REFERENCES

[1]D. M. Goebel and I. Katz, Fundamentals of Electric Propulsion: Ion and Hall Thrusters, JPL space science and technology series (Wiley, 2008).

[2]E. Y. Choueiri, "Plasma oscillations in Hall thrusters," Physics of Plasmas **8**, 1411 (2001).

[3]J.-P. Boeuf and A. Smolyakov, "Physics and instabilities of low-temperature E × B plasmas for spacecraft propulsion and other applications," Physics of Plasmas **30** (2023), 10.1063/5.0145536.

[4]T. Lafleur, S. D. Baalrud, and P. Chabert, "Theory for the anomalous electron transport in Hall effect thrusters. II. Kinetic model," Physics of Plasmas **23**, 053503 (2016).

[5]A. I. Smolyakov, O. Chapurin, W. Frias, O. Koshkarov, I. Romadanov, T. Tang, M. Umansky, Y. Raitses, I. D. Kaganovich, and V. P. Lakhin, "Fluid theory and simulations of instabilities, turbulent transport and coherent structures in partially-magnetized plasmas of E × B discharges," Plasma Physics and Controlled Fusion **59**, 014041 (2017).

[6]F. Petronio, A. Tavant, T. Charoy, A. Alvarez Laguna, A. Bourdon, and P. Chabert, "Conditions of appearance and dynamics of the modified two-stream instability in E × B discharges," Physics of Plasmas **28**, 043504 (2021).

[7]F. Petronio, T. Charoy, A. Alvarez Laguna, A. Bourdon, and P. Chabert, "Two-dimensional effects on electrostatic instabilities in hall thrusters. i. insights from particle-in-cell simulations and two-point power spectral density reconstruction techniques." Physics of Plasmas (2023), 10.1063/5.0119253.

[8]F. Petronio, T. Charoy, A. Alvarez Laguna, A. Bourdon, and P. Chabert, "Two-dimensional effects on electrostatic instabilities in hall thrusters. ii. comparison of particle-in-cell simulation results with linear theory dispersion relations." Physics of Plasmas (2023), 10.1063/5.0119255.

[9]J. Boeuf and L. Garrigues, "Low frequency oscillations in a stationary plasma thruster," Journal of Applied Physics **84**, 3541–3554 (1998).

[10]J. Fife, M. Martinez-Sanchez, and J. Szabo, "A numerical study of low-frequency discharge oscillations in hall thrusters," in 33rd Joint Propulsion Conference and Exhibit (1997) p. 3052.

[11]A. I. Morozov and V. V. Savelyev, Fundamentals of stationary plasma thrusters theory (Springer, 2000).

[12]K. Hara, M. J. Sekerak, I. D. Boyd, and A. D. Gallimore, "Perturbation analysis of ionization oscillations in Hall effect thrusters," Physics of Plasmas **21**, 122103 (2014).

[13]E. T. Dale, B. Jorns, and K. Hara, "Numerical investigation of the stability criteria for the breathing mode in Hall Effect Thrusters," (35nd International Electric Propulsion Conference - Atlanta, Georgia, USA, 2017).

[14]T. Lafleur, P. Chabert, and A. Bourdon, "The origin of the breathing mode in Hall thrusters and its stabilization," Journal of Applied Physics **130**, 053305 (2021).

[15]S. Chable and F. Rogier, "Numerical investigation and modeling of stationary plasma thruster low frequency oscillations," Physics of Plasmas **12**, 033504 (2005).

[16]S. Barral and E. Ahedo, "Low-frequency model of breathing oscillations in Hall discharges," Physical Review E **79**, 046401 (2009).

[17]S. Barral and Z. Peradzynski, "Ionization oscillations in Hall accelerators," Physics of Plasmas **17**, 014505 (2010).

[18]O. Chapurin, A. I. Smolyakov, G. Hagelaar, and Y. Raitses, "On the mechanism of ionization oscillations in Hall thrusters," Journal of Applied Physics **129**, 233307 (2021).

[19]O. Chapurin, A. I. Smolyakov, G. Hagelaar, J.-P. Boeuf, and Y. Raitses, "Fluid and hybrid simulations of the ionization instabilities in Hall thruster," Journal of Applied Physics **132**, 053301 (2022).

[20]M. Reza, F. Faraji, A. Knoll, A. Piragino, T. Andreussi, and T. Misuri, "Reduced-order particle-in-cell simulations of a high-power magnetically shielded hall thruster," Plasma Sources Science and Technology (2023), 10.1088/1361-6595/acdea3.

[21]D. Maddaloni, A. Domínguez-Vázquez, F. Terragni, and M. Merino, "Data-driven analysis of oscillations in Hall thruster simulations," Plasma Sources Science and Technology **31**, 045026 (2022).

[22]Y. B. Esipchuk, A. Morozov, G. Tilinin, and A. Trofimov, "Plasma oscillations in closed-drift accelerators with an extended acceleration zone," Soviet Physics Technical Physics **18**, 928 (1974).

[23]N. Gascon, M. Dudeck, and S. Barral, "Wall material effects in stationary plasma thrusters. I. Parametric studies of an SPT-100," Physics of Plasmas **10**, 4123–4136 (2003).

[24]V. Giannetti, M. M. Saravia, and T. Andreussi, "Measurement of the breathing mode oscillations in Hall thruster plasmas with a fast-diving triple Langmuir probe," Physics of Plasmas **27**, 123502 (2020).

[25]E. T. Dale and B. A. Jorns, "Experimental characterization of hall thruster breathing mode dynamics," Journal of Applied Physics **130**, 133302 (2021).

[26]L.-Q. Wei, L. Han, D.-R. Yu, and N. Guo, "Low-frequency oscillations in Hall thrusters," Chi-

nese Physics B **24**, 055201 (2015).

[27]T. Charoy, T. Lafleur, A. A. Laguna, A. Bourdon, and P. Chabert, "The interaction between ion transit-time and electron drift instabilities and their effect on anomalous electron transport in Hall thrusters," Plasma Sources Science and Technology **30**, 065017 (2021).

[28]J. P. Boeuf and L. Garrigues, "E × B electron drift instability in Hall thrusters: Particle-in-cell simulations vs. theory," Physics of Plasmas **25**, 061204 (2018).

[29]T. Charoy, J. P. Boeuf, A. Bourdon, J. A. Carlsson, P. Chabert, B. Cuenot, D. Eremin, L. Garrigues, K. Hara, I. D. Kaganovich, A. T. Powis, A. Smolyakov, D. Sydorenko, A. Tavant, O. Vermorel, and W. Villafana, "2D axial-azimuthal particle-in-cell benchmark for low-temperature partially magnetized plasmas," Plasma Sources Science and Technology **28**, 105010 (2019).

[30]W. Villafana, F. Petronio, A. C. Denig, M. J. Jimenez, D. Eremin, L. Garrigues, F. Taccogna, A. Alvarez-Laguna, J. P. Boeuf, A. Bourdon, P. Chabert, T. Charoy, B. Cuenot, K. Hara, F. Pechereau, A. Smolyakov, D. Sydorenko, A. Tavant, and O. Vermorel, "2D radial-azimuthal particle-in-cell benchmark for E × B discharges," Plasma Sources Science and Technology **30**, 075002 (2021).

[31]V. Croes, T. Lafleur, Z. Bonaventura, A. Bourdon, and P. Chabert, "2D particle-in-cell simulations of the electron drift instability and associated anomalous electron transport in Hall-effect thrusters," Plasma Sources Science and Technology **26**, 034001 (2017).

[32]T. Charoy, T. Lafleur, A. Tavant, P. Chabert, and A. Bourdon, "A comparison between kinetic theory and particle-in-cell simulations of anomalous electron transport in E × B plasma discharges," Physics of Plasmas **27**, 063510 (2020).

[33]V. Vahedi and M. Surendra, "A Monte Carlo collision model for the particle-in-cell method: applications to argon and oxygen discharges," Computer Physics Communications **87**, 179–198 (1995).

[34]E. F. Toro, Riemann solvers and numerical methods for fluid dynamics: a practical introduction, 2nd ed. (Springer-Verlag, Berlin ; New York, 1999).

[35]Z. Zhang, Z. Zhang, H. Tang, W. Y. L. Ling, Z. Chen, J. Ren, and J. Cao, "Measurement of the distribution of charge exchange ions in a hall-effect thruster plume," Plasma Sources Science and Technology **29**, 085001 (2020).

[36]C. Birdsall, "Particle-in-cell charged-particle simulations, plus Monte Carlo collisions with neutral atoms, PIC-MCC," IEEE Transactions on Plasma Science **19**, 65–85 (1991).

[37]F. Petronio, Plasma instabilities in Hall Thrusters: a theoretical and numerical study, Ph.D. the-

sis, Ecole Polytechnique (2023), 2023IPPAX030.

[38]D. Bohm, "The use of probes for plasma exploration in strong magnetic fields," Characteristics of Electrical Discharges in Magnetic Fields **13** (1949).

[39]P. Chabert and N. Braithwaite, Physics of Radio-Frequency Plasmas (Cambridge University Press, 2011).

[40]P. Coche and L. Garrigues, "A two-dimensional (azimuthal-axial) particle-in-cell model of a Hall thruster," Physics of Plasmas **21**, 023503 (2014).

[41]G. Fubiani, L. Garrigues, G. Hagelaar, N. Kohen, and J. P. Boeuf, "Modeling of plasma transport and negative ion extraction in a magnetized radio-frequency plasma source," New Journal of Physics **19**, 015002 (2017).

[42]F. Petronio, A. Alvarez Laguna, A. Bourdon, and P. Chabert, "The introduction of a virtual radial direction in axial-azimuthal PIC simulations of Hall Thrusters," in 37th International Electric Propulsion Conference (Boston, Massachussets, 2022).

[43]A. A. Litvak and N. J. Fisch, "Resistive instabilities in Hall current plasma discharge," Phys. Plasmas **8**, 5 (2001).

[44]O. Koshkarov, A. I. Smolyakov, I. V. Romadanov, O. Chapurin, M. V. Umansky, Y. Raitses, and I. D. Kaganovich, "Current flow instability and nonlinear structures in dissipative two-fluid plasmas," Physics of Plasmas **25**, 011604 (2018).

[45]T. Ito, N. Gascon, W. S. Crawford, and M. A. Cappelli, "Experimental Characterization of a Micro-Hall Thruster," Journal of Propulsion and Power **23**, 1068–1074 (2007).

[46]R. Lobbia, B. and A. D. Gallimore, "Two-dimensional Time-resolved Breathing Mode Plasma Fluctuation Variation with Hall Thruster Discharge Settings," (2009).

[47]A. Jardin, M. Jakubczak, A. Riazantsev, A. Jardin, J. Kurzyna, and P. Lubiński, "Searching for Chaotic Behavior in the Ion Current Waveforms of a Hall Effect Thruster," Journal of Fusion Energy **41**, 20 (2022).